NATIONAL TECHNICAL UNIVERSITY OF ATHENS

DIPLOMA THESIS

Dynamic Analysis of Jet Engine Rotors including Nonlinearities by Advanced Squeeze Film Damper and Ball Bearing Models utilizing Harmonic Balance Method

Author:

Vasileios Veloudis

Supervisor:

Athanasios Chasalevris

A thesis submitted in fulfillment of the requirements
for the degree of Diploma in Mechanical Engineering

Athens, January 2024

Έχω διαβάσει και κατανοήσει τους κανόνες για τη λογοκλοπή και τον τρόπο σωστής αναφοράς των πηγών που περιέχονται στον οδηγό συγγραφής Διπλωματικών Εργασιών. Δηλώνω ότι, από όσα γνωρίζω, το περιεχόμενο της παρούσας Διπλωματικής Εργασίας είναι προϊόν δικής μου εργασίας και υπάρχουν αναφορές σε όλες τις πηγές που χρησιμοποίησα.

Οι απόψεις και τα συμπεράσματα που περιέχονται σε αυτή τη Διπλωματική εργασία είναι του συγγραφέα και δεν πρέπει να ερμηνευθεί ότι αντιπροσωπεύουν τις επίσημες θέσεις της Σχολής Μηχανολόγων Μηχανικών ή του Εθνικού Μετσόβιου Πολυτεχνείου.

Βασίλειος Βελούδης

Acknowledgements

First of all, I would like to sincerely thank my professor Athanasios Chasalevris for his continuous advice and valuable remarks throughout the project. This thesis wouldn't be possible without him.

My deepest gratitude goes to my supervisor at MTU Aero Engines, Dr. Ioannis Chatzisavvas. His excellent guidance and character made it a privilege to work with him. He was truly there for anything I needed. I cannot thank him enough.

I would also like to thank the entire Rotordynamics team for the excellent collaboration. Special thanks to Ino and Felix for their support on parts of the project.

Finally, a big thank you to my family, my friends in Greece and N. for their continued support, and to the new friends I made in Munich who made this experience unforgettable.

Abstract

A jet engine must perform optimally both in the thrust and efficiency categories as well as in the vibration behavior. Excessive vibration levels can compromise the structural integrity of the engine and increase the noise level perceived by the passengers of the aircraft. Therefore, efficient and detailed modeling of the dynamic behavior of the entire engine is of paramount importance.

This thesis implements the Harmonic Balance Method with an appropriate condensation technique to efficiently simulate the dynamic performance of a generic, whole engine model in the frequency domain. The novelty of the work lies in the application of the method to whole engine models using not only the short squeeze film damper (SFD) approximation for the calculation of the nonlinear reaction forces but also state-of-the-art approaches developed in recent years. In addition, the work also integrates ball bearing models into the simulations, providing results where the entire SFD configuration is modeled. Similar studies on whole engine simulations in the frequency domain are not yet found in the literature.

Through an extensive series of simulations, the study identifies critical simulation and design considerations. The significance of the zero harmonic is emphasized and its replacement by static analysis is challenged. The collaborative design approach, which aligns the stiffness of the SFD support to the desired response, emerges as a critical factor. Furthermore, detailed SFD models reveal the impact of fluid inertia modeling on the dynamic response of the engine, especially when a feed groove is present. The inclusion of ball bearing models also seems to affect the system response, although, for the specific case examined, a fine-tuned stiffness value could be used for the early design stages.

Through a collaborative effort, the study extends into the realm of surrogate modeling, demonstrating how various predictive models have the potential to be integrated into nonlinear dynamic simulations as a cost-effective alternative.

Collectively, all of the findings enhance the understanding of the intricate relationship between squeeze film dampers, rolling element bearings and the overall system response, providing insights and considerations for efficient jet engine design.

Abstract (in Greek)

Ένας αεριωθούμενος (jet) κινητήρας πρέπει να αποδίδει βέλτιστα τόσο στις κατηγορίες ώσης και απόδοσης όσο και στη ταλαντωτική συμπεριφορά. Τα υπερβολικά επίπεδα κραδασμών μπορούν να θέσουν σε κίνδυνο τη δομική ακεραιότητα του κινητήρα και να αυξήσουν το επίπεδο θορύβου που γίνεται αντιληπτό από τους επιβάτες του αεροσκάφους. Ως εκ τούτου, η αποτελεσματική και λεπτομερής μοντελοποίηση της δυναμικής συμπεριφοράς ολόκληρου του κινητήρα είναι υψίστης σημασίας.

Η παρούσα εργασία εφαρμόζει τη Μέθοδο Αρμονικής Ισορροπίας με μια κατάλληλη τεχνική συμπύκνωσης για την αποτελεσματική προσομοίωση της δυναμικής συμπεριφοράς ενός γενικευμένου, ολόκληρου μοντέλου κινητήρα αεροσκάφους στο πεδίο της συχνότητας. Η καινοτομία της εργασίας έγκειται στην εφαρμογή της μεθόδου σε ολόκληρα μοντέλα κινητήρα, χρησιμοποιώντας όχι μόνο την προσέγγιση του κοντού αποσβεστήρα συμπιεσμένου ελαίου (ΑΣΕ) για τον υπολογισμό των μη γραμμικών δυνάμεων αντίδρασης, αλλά και σύγχρονες προσεγγίσεις που έχουν αναπτυχθεί τα τελευταία χρόνια. Επιπλέον, η εργασία ενσωματώνει και μοντέλα εδράνων κύλισης (ρουλεμάν) στις προσομοιώσεις, παρέχοντας αποτελέσματα όπου μοντελοποιείται ολόκληρη η διαμόρφωση του ΑΣΕ. Παρόμοιες μελέτες για προσομοιώσεις ολόκληρου του κινητήρα στο πεδίο της συχνότητας δεν έχουν ακόμη βρεθεί στη βιβλιογραφία.

Μέσω μιας εκτεταμένης σειράς προσομοιώσεων, η μελέτη εντοπίζει κρίσιμα ζητήματα προσομοίωσης και σχεδιασμού. Η σημασία της μηδενικής αρμονικής τονίζεται και η αντικατάστασή της από τη στατική ανάλυση αμφισβητείται. Η προσέγγιση συνεργατικού σχεδιασμού, η οποία ευθυγραμμίζει την δυσκαμψία της στήριξης του ΑΣΕ με την επιθυμητή απόκριση, αναδεικνύεται ως κρίσιμος παράγοντας. Επιπλέον, λεπτομερή μοντέλα ΑΣΕ αποκαλύπτουν την επίδραση της μοντελοποίησης της αδράνειας του ρευστού στη δυναμική απόκριση του κινητήρα, ιδίως όταν υπάρχει αυλάκι τροφοδοσίας. Η συμπερίληψη μοντέλων ρουλεμάν φαίνεται επίσης να επηρεάζει την απόκριση του συστήματος, αν και, για τη συγκεκριμένη περίπτωση που εξετάστηκε, θα μπορούσε να χρησιμοποιηθεί μια ρυθμισμένη τιμή δυσκαμψίας για τα πρώτα στάδια σχεδιασμού.

Μέσω μιας συνεργατικής προσπάθειας, η μελέτη επεκτείνεται στον τομέα της παρένθετης μοντελοποίησης, αποδεικνύοντας πώς διάφορα μοντέλα πρόβλεψης έχουν τη δυνατότητα να ενσωματωθούν σε μη-γραμμικές δυναμικές προσομοιώσεις ως μια οικονομικά-αποδοτική εναλλακτική λύση.

Συλλογικά, όλα τα ευρήματα ενισχύουν την κατανόηση της περίπλοκης σχέσης μεταξύ των αποσβεστήρων συμπιεσμένου ελαίου, των εδράνων κύλισης και της συνολικής απόκρισης του συστήματος, παρέχοντας πληροφορίες και σκέψεις για τον αποτελεσματικό σχεδιασμό αεριωθούμενων κινητήρων.

Contents

List of Figures

List of Tables

List of Symbols

Arrays/vectors are represented by bold lowercase letters and matrices by bold uppercase letters. The following list contains only the most common symbols used throughout the thesis. Additional symbols or symbols with different meanings are clearly indicated. The terms vector and array are used interchangeably.

Latin symbols

$\mathbf{C}$	Structural damping matrix
$\mathbf{C_{visc}}$	Viscous damping matrix
$\tilde{\mathbf{C}}$	Partitioned structural damping matrix
$\mathbf{D}$	Viscous damping/gyroscopic matrix
$\tilde{\mathbf{D}}$	Partitioned viscous damping/gyroscopic matrix
$\mathbf{f}$	Force array
$\mathbf{G}$	Gyroscopic matrix
h	Oil film thickness
j	Imaginary unit
$\mathbf{K}$	Stiffness matrix
$\tilde{\mathbf{K}}$	Partitioned stiffness matrix
k	Harmonic index
$\mathbf{M}$	Mass matrix
$\tilde{\mathbf{M}}$	Partitioned mass matrix
m	Order of the Fourier series
n	Total number of degrees of freedom
p	Number of linear degrees of freedom
q	Number of nonlinear degrees of freedom
$\mathbf{r}$	Solution array
t	Time

$\mathbf{x}$	Displacement vector
$\dot{\mathbf{x}}$	Velocity vector
$\ddot{\mathbf{x}}$	Acceleration vector
$\mathbf{0}$	Zero array

Greek symbols

$\boldsymbol{\alpha}$	Fourier coefficient array - real component
$\boldsymbol{\beta}$	Fourier coefficient array - imaginary component
ω	Rotational speed

Subscripts and Superscripts

$(...)_{\mathbf{g}}$	Gravity
$(...)_{\mathbf{k}}$	k-th harmonic
$(...)_{\mathbf{u}}$	Unbalance
$(...)_{\mathbf{0}}$	Zero harmonic
$(...)^{\mathrm{p}}$	p linear degrees of freedom
$(...)^{\mathrm{q}}$	q nonlinear degrees of freedom

Abbreviations

BW	Backward Whirling
FEM	Finite Element Method
FW	Forward Whirling
HP	High Pressure
HPC	High Pressure Compressor
HPC-S1	High Pressure Compressor - 1st stage
HPT	High Pressure Turbine
HPT-S1	High Pressure Turbine - 1st stage
LP	Low Pressure
LPC	Low Pressure Compressor
LPC-S1	Low Pressure Compressor - 1st stage

LPT	Low Pressure Turbine
LPT-S1	Low Pressure Turbine - 1st stage
REB	Rolling Element Bearing
RHS	Right-Hand Side
rpm	Revolutions Per Minute
SFD	Squeeze Film Damper
SQC	Squirrel Cage

1 Introduction

1.1 Jet Engine Overview

Jet engines belong to the broader category of aircraft engines, which are used to develop thrust and power various types of aircraft. The main characteristic that distinguishes them from the various types of aircraft engines is that they provide thrust through the principle of jet propulsion. In essence, a stream of hot gas is generated by combustion and later expanded through a nozzle configuration that increases its velocity and forms the propulsive jet [62]. There are four main components found in such engines: a compressor, a combustion chamber, a turbine and a nozzle.

Depending on the configuration, a jet engine can be further classified as a turbojet or a turbofan engine, as shown in Figure 1.1. In a turbojet engine, all of the intake air is compressed by the compressor and later ignited in the combustion chamber with the addition of an appropriate fuel. The resulting hot exhaust gas expands in the turbine, which drives the compressor, and is then directed into the exhaust nozzle, which increases its velocity and creates the propulsive jet. Since thrust depends solely on jet flow, higher temperatures are required in the combustion chamber and thus the compressor must pressurize the intake air to significant levels. For this reason, the addition of an afterburner after the turbine is common practice in turbojets [64]. Additional fuel is injected into the hot gas stream, which is reignited to produce more thrust without overloading the compressor. Due to high operating costs and high exhaust velocities, they are most commonly used in military applications.

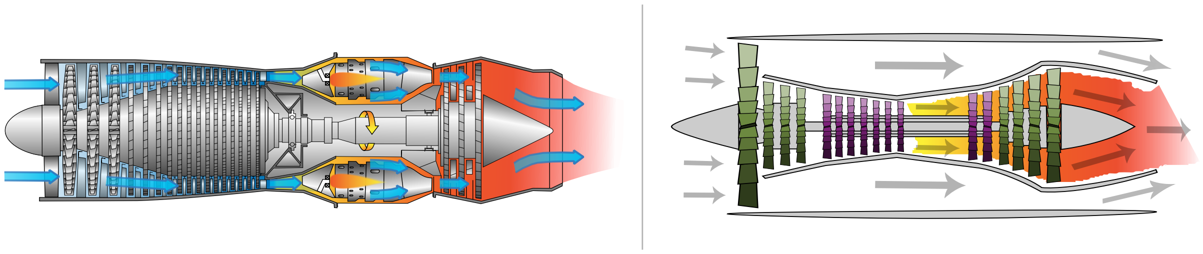

Figure 1.1: Diagram of a typical turbojet (left) and a turbofan (right) engine configuration. Adapted from [64].

The turbofan engine works on a similar principle, with the difference being in the presence of a fan in the intake of the engine. The premise behind its presence is that the thrust increases with airflow rate when the fuel consumption rate stays constant [31, 17]. Behind the fan, the inlet stream is divided into a hot and a cold stream. The former passes through the core of the engine, which essentially acts as a turbojet, while the latter bypasses the core and is accelerated. In turbofan engines, the thrust comes mainly from this secondary flow, while the core is used primarily to drive the rest of the components. Turbofan engines offer lower fuel consumption and quieter operation compared to turbojet engines and are therefore the dominant choice in the commercial aviation industry [14].

Jet engines can have multiple spools, or shafts, rotating in the same or opposite directions. Each shaft/rotor is responsible for driving different components of the engine. The most common configuration found is the dual or twin-spool engine. In this case, the fan is usually connected to the low pressure compressor (LPC) and low pressure turbine (LPT) on the same shaft, which is called the low pressure rotor (LPR) [40]. In addition, there is a high pressure rotor (HPR) linking the high pressure compressor (HPC) with the high pressure turbine (HPT). One of the most successful dual-spool engines manufactured is the CFM56 [66]. Less common are three-spool configurations. An example of such a configuration is the Trent 1000 engine by Rolls-Royce. Multiple spools provide better power distribution, enhanced thrust control and improved efficiency and are therefore very common in modern aircraft.

1.2 Beyond Propulsion: Vibrations and Bearings in Jet Engines

While thrust generation and thermal efficiency are primary concerns in the design of a jet engine, vibrations resulting from the dynamic interaction of components are also an important design consideration. Large vibrations can compromise the integrity of the engine structure, causing cyclic stresses and fatigue failures in engine components, structural damage to the rotor bearings and collisions of the rotor with stationary parts [43]. The latter, resulting in blade damage, also significantly reduces the overall efficiency of the engine. In addition, vibrations in the engine are directly related to noise and can be transmitted through the aircraft structure to the fuselage, causing discomfort to passengers [20, 16]. Therefore, the dynamic analysis of the engine in order to study and reduce vibrations is of paramount importance.

A solid foundation for the dynamic analysis of rotating machinery can be found in the work of Friswell [19], who also studied the dynamics of dual-spool configurations. Today, increased computing power has allowed engineers to employ numerical methods to efficiently model and simulate the dynamic behavior of the engine. The most commonly used approach is the Finite Element Method (FEM), which divides the engine into multiple finite elements. The choice between the types of elements is vast, but the simplest and most commonly used is the one-dimensional Timoshenko beam element [60, 61, 13]. A more detailed presentation of the modeling of jet engines can be found in [44], as well as in Chapter 4.

One of the most important components in vibration control is the bearing. Their type, location and design have a tremendous effect on the dynamic response and stability of a rotating system, as can be seen from the extensive literature on the subject. The most commonly used types are journal and rolling element bearings (REBs). Each has advantages and disadvantages that make them suitable for different applications. Journal bearings are widely used in machinery belonging to the power, oil, gas and petrochemical industries, as well as in the automotive industry [7]. Some of their advantages include quiet operation and gradual wear, which means they are not susceptible to sudden failure. However, they are characterized by high frictional forces, their life cycle is not easy to calculate and they show unstable operation under certain conditions [48]. However, there is a significant amount of literature that examines these instabilities and how they can be addressed through improved, tunable designs [12, 21, 1]. Due to these disadvantages, the aviation industry relies solely on rolling element bearings [38], although their range of applications is also vast. Their lower load capacity compared to journal bearings is compensated by their low friction losses, higher speed applicability, low cost and thrust load capacity [48]. An example of their dominant presence in a jet engine is highlighted in Fig. 1.2, which shows the location and type of the eight bearings in the Trent 1000 engine.

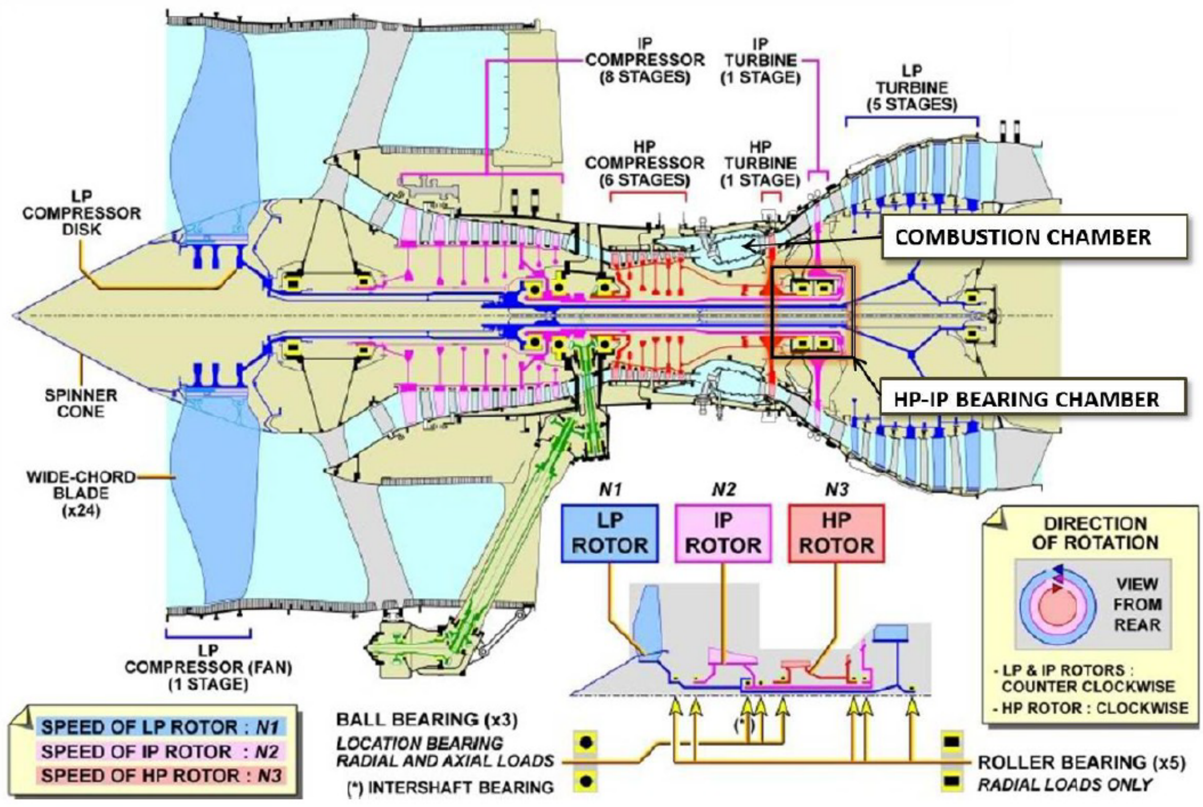

Figure 1.2: Bearings of the Rolls-Royce Trent 1000 engine [54]

Although rolling element bearings are used extensively in jet engines, the damping they provide is not sufficient to reduce vibration amplitudes. Therefore, one or more of the bearings in the engine are placed in series with a squeeze film damper (SFD). Essentially, the rotating shaft is mounted on the bearing and the outer race is not allowed to rotate. These two components together form the journal. Between the journal and the SFD housing is a clearance filled with lubricant. Since the rotation of the shaft is decoupled from the motion of the journal by the presence of the rolling elements, the motion of the journal caused by the vibration of the shaft is converted into a pure whirl motion. This results in the squeezing of the lubricant film and the generation of reaction forces. These forces provide the damping that the bearing cannot provide on its own. A typical

SFD configuration is shown on the left side of Fig. 1.3. Depending on the application, a SFD can also be supported by a squirrel cage (SQC), which carries the weight of the configuration and keeps the SFD centered. If the SFD is not supported, the journal will be in direct contact with the housing at the start of operation.

Since the SFD reaction forces are the source of the external damping of the system, their accurate prediction is crucial for the dynamic design of the engine. In the experimental field, a lot of research has been conducted to investigate the effects of different geometric and operational characteristics on the performance of the damper. One of the most important experimental initiatives has been the collaboration between Texas A& M University and an aircraft engine manufacturer, led by San Andres. In this work, damping and added mass coefficients are calculated for different amplitude motions and static eccentricity positions and compared with the available literature [3]. Among a plethora of results, the authors highlight the importance of the fluid film inertia, which generates significant added mass and contributes to the reaction forces. Additionally, contrary to common belief, they show that the feed groove often found in SFDs does not isolate the damper into two separate parts. Due to the incompressibility of the oil, fluid inertia effects become important and are the reason why large dynamic pressures are generated. This effect increases the damping reaction force [2]. The effect of the sealing arrangement in the SFD is also examined as part of this work. It was found that compared to an open-ends damper, sealing increases the damping performance. Common sealing approaches are the piston-ring seal and the O-ring seal, with the former being preferred in jet engine applications [4, 51]. A visual representation of the feed groove and piston ring seal can be seen on the right side of Fig. 1.3.

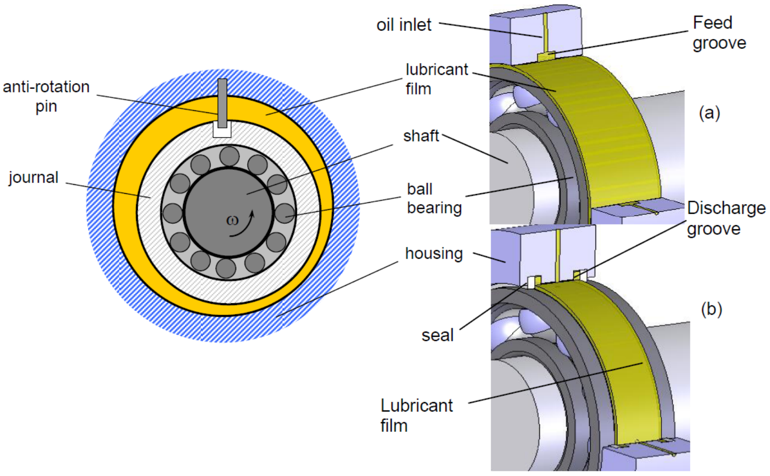

Figure 1.3: Typical squeeze film damper (SFD) configuration (left) with feed groove and piston ring sealing (right). [22]

In the field of SFD modeling, the simplest approach to calculate the reaction forces of the damper is to apply the short-bearing approximation to the Reynolds equation and calculate analytical expressions for the reaction forces in both directions. A very detailed derivation of these formulas can be found in the work of Mitsos [44]. This model is very computationally efficient, but it does not take into account inertial effects and complex geometric features that significantly affect SFD performance. Hori [32] lays a solid foundation for the calculation of these forces, taking into account the inertial contribution as well, but still implementing the short-bearing approximation in the Reynolds equation to arrive at an analytical expression. In the work of Karimulla et al. [35] and Hamzehlouia and Behdinan [29], the authors also use the short-bearing SFD, but go a step further and include both temporal and convective inertia terms before arriving at the analytical force expressions.

Today, state-of-the-art models have been developed to accurately predict these forces. The common feature of these models is that the Reynolds equation is now solved numerically. This is referred to as finite bearing modeling. A detailed review of the state of the art is presented by Gheller et al. [22, 23]. In particular, the inclusion of oil film cavitation, air ingestion and inertia effects are discussed and a finite element approach is presented. More specifically, in terms of inertia modeling, the work of San Andres and Delgado [6] introduces the temporal inertia term and presents a finite element solution for the resulting modified Reynolds equation. The most detailed model in terms of inertia is completed with the inclusion of convective inertia, which is described in the work of Hamzehlouia [27].

Regarding the oil temperature, the usual approach is to consider it as a constant value. However, during operation, the oil is squeezed by the journal and absorbs vibration energy, which due to the internal friction in the oil film, causes a significant increase in its temperature [67]. Thus, in reality, the oil temperature varies. In recent years, this effect has led to the development of thermohydrodynamic (THD) SFD models that account for this temperature variation. Perreault et al. [46] develop a CFD model to investigate such THD effects in SFDs and conclude that the temperature of the lubricant increases as the whirl frequency, eccentricity ratio and SFD radial clearance increase. The same behavior is observed in the work of Hamzehlouia and Behdinan [28], who developed a THD SFD model that includes the inertial effect of the lubricant film.

1.3 Simulating Jet Engine Dynamics: Overview and Motivation

As the modeling of SFDs becomes more detailed, the question arises as to how they affect the dynamic response of jet engines. Since a transient simulation is often extremely time consuming, there are numerous studies that use the Harmonic Balance Method (HBM) to obtain the steady-state solution of the equation of motion in the frequency domain. The vast majority of these studies simulate single rotor configurations and use short SFD models, some more detailed than others [45, 55]. However, the classical HBM approach becomes computationally inefficient for large systems with hundreds or thousands of degrees of freedom. Therefore, it cannot be used to simulate whole engine models and becomes even less efficient when detailed, state-of-the-art SFD models need to be integrated, which in themselves increase computational time.

Pioneering work in the simulation of whole engine models was done by Bonello and Pham [9, 47, 8]. The authors developed the Receptance Harmonic Balance Method (RHBM) and the Impulsive Receptance Method (IRM) for efficient calculation of the response of such models in the frequency and time domains respectively, leveraging the fact that a jet engine has only a small number of truly nonlinear degrees of freedom.

These nonlinearities arise from SFDs and rolling element bearings and can significantly increase the simulation time if the entire system is solved as nonlinear. Regarding the frequency domain simulation, the RHBM uses information extracted from the eigenvalue analysis of the linear part of the engine to set up the system for the nonlinear component. As a result, the size of the vector of unknowns is drastically reduced. The authors also applied the RHBM for a realistic three-spool engine configuration for the case of multiple unbalance excitation, which occurs when the unbalance is located on more than one rotor [26]. However, the SFD model implemented used the λ-Theory to derive simple, analytical formulas for the pressure field under short and long SFD assumptions.

The concept of segregating a system into a primary and a secondary component in order to reduce simulation time was known long before the work of the aforementioned authors. In 1978, the idea of the dynamic condensation was presented [39]. However, the first time it was applied to a rotor dynamic analysis was in 1994 by Hahn and Chen [25]. The authors applied the method to simple FEM rotor models supported on SFDs and developed an improved Harmonic Balance Method where the nonlinear system is solved only for the truly nonlinear degrees of freedom. During the condensation procedure, a linear system appeared that was used to approximate the response of the linear component. This method showed a tremendous simulation improvement compared to the classic HBM and this is why many studies that followed employed it to simulate more complex rotor systems. Sinou [56] implemented the HBM using appropriate dynamic condensation to simulate the nonlinear response of a flexible rotor supported by ball bearings. The ball bearing models used were based on Hertzian contact theory to calculate the nonlinear reaction force. He et al. [30] applied the method to a realistic low pressure rotor of a jet engine supported on SFDs and compared various results with transient simulations. The SFD modeling used the short-bearing approach with appropriate boundary conditions to simulate a piston ring seal. The authors observed almost negligible differences with the transient analysis result, while the HBM was 5 to 12 times faster.

It can be concluded that the majority of the studies using the HBM share some common characteristics. The model of the SFD being used is relatively simple, nonlinear ball bearing models connected in series with a nonlinear SFD spring are not implemented and, excluding the work of Bonello and Pham, no whole engine models are being simulated. The author of this thesis recognizes the great potential of the HBM using dynamic condensation and observes the need for state-of-the-art SFD models as well as nonlinear ball bearing models to be integrated into nonlinear simulations of whole jet engine models.

A concise overview of the chapters is provided to give a clearer insight into the content of the thesis:

In **Chapter 2**, the classical HBM method is presented and the mathematical basis of the method is explained. Then, the dynamic condensation is applied and the reduced nonlinear system for the nonlinear degrees of freedom is derived in detail. Important parts of its solution procedure are explained and the schematic representation of the algorithm is shown. Finally, the approach for dealing with the dual unbalance excitation in this thesis is presented.

In **Chapter 3**, the nonlinear modeling of the squeeze film damper and the rolling element bearing is briefly discussed, since the aim of this thesis was not to delve deep into their modeling but rather to understand the differences between each model and integrate them into rotor dynamic simulations. The equations governing the short SFD approach are shown and then the state-of-the-art models are described, where the modified Reynolds equation is presented to include the temporal inertia term. In addition, the main equations used in a THD SFD model are given with a brief explanation. Finally, two different models for calculating the nonlinear ball bearing reaction forces are explained.

In **Chapter 4**, the HBM with appropriate dynamic condensation is applied to a generic jet engine model with a dual-spool configuration. The model includes one SFD supported by a squirrel cage (SQC). In the beginning, the usefulness of the SFD is investigated by examining which resonance amplitudes it can attenuate through an eigenvalue/linear analysis. The results of the linear analysis are compared with the nonlinear simulations using the short SFD. An unbalance is then placed on both rotors of the engine to simulate a dual unbalance excitation. Keeping the simple SFD model, the effects of oil temperature, radial clearance size, SQC support stiffness and maneuvering loads on the dynamic response of the engine are investigated. Then, the state-of-the-art SFD models are integrated and the effects of different oil cavitation conditions, fluid inertia and the presence and geometry of feed grooves are studied. Finally, nonlinear simulations using the short SFD and two different ball bearing models are presented. The results are compared with nonlinear simulations using the short SFD and three constant stiffness values for the ball bearing spring.

In **Chapter 5**, a collaborative work on the potential of the improved HBM for training surrogate models for fast dynamic predictions is showcased. Using neural networks, three surrogate models are trained, each with a specific function and with increasing accuracy. Using these models, various results are obtained and discussed.

In **Chapter 6**, the main conclusions of the thesis are presented along with recommendations for the next steps in the research.

2 The Harmonic Balance Method in Nonlinear Rotor Dynamics

In this section, the Harmonic Balance Method (HBM) is introduced along with a dynamic condensation for great improvements in simulation efficiency.

2.1 Nonlinear Equations of Motion

An aircraft engine model can be represented as a system of second-order ordinary differential equations using the Finite Element Method. The solution of these equations describes the motion of the system under a given load and thus they are referred to as equations of motion (EOM). In the general case where the external load is both linear and nonlinear, they take the following form:

$$\mathbf{M} \cdot \ddot{\mathbf{x}} + \mathbf{D} \cdot \dot{\mathbf{x}} + \mathbf{K} \cdot \mathbf{x} = \mathbf{f}\left(\mathbf{x}, \dot{\mathbf{x}}, \ddot{\mathbf{x}}, \omega, t\right) \tag{2.1}$$

where $\mathbf{M}$ is the mass matrix, $\mathbf{D} = \omega\mathbf{G} + \mathbf{C_{visc}}$ is the gyroscopic and viscous damping matrix and $\mathbf{K}$ is the stiffness matrix. Linear stiffness and viscous damping bearing matrices are also included.

The linear force component is due to unbalance excitation and weight acting on the system, whereas the nonlinear component in this analysis is due to squeeze film damper (SFD) and rolling element bearing (REB) reaction forces. When the EOM is being solved in the frequency domain, it is possible to include an imaginary stiffness term to account for the structural damping $\mathbf{C}$. The EOM then becomes:

$$\mathbf{M} \cdot \ddot{\mathbf{x}} + \mathbf{D} \cdot \dot{\mathbf{x}} + \left(\mathbf{K} + j\mathbf{C}\right) \cdot \mathbf{x} = \mathbf{f}\left(\mathbf{x}, \dot{\mathbf{x}}, \ddot{\mathbf{x}}, \omega, t\right) \tag{2.2}$$

2.2 Classic Harmonic Balance Method

The Harmonic Balance Method (HBM) is an approach to solving nonlinear problems in the frequency domain when the forcing is periodic. The nonlinear force on the right-hand side (RHS) of Eq. 2.2 is assumed to be of this nature and thus it can be expressed as a truncated Fourier series with a fundamental frequency of ω. The RHS also includes an additional zero order excitation due to the weight and a first order excitation due to the unbalance. Therefore, the RHS can be expressed as:

$$\mathbf{f}\left(\mathbf{x},\dot{\mathbf{x}},\ddot{\mathbf{x}},\omega,t\right)=\mathbf{f_{0,NL}}+\sum_{k=1}^{m}\mathbf{f_{k,NL}}e^{jk\omega t}+\mathbf{f_g}+\mathbf{f_u}e^{j\omega t} \tag{2.3}$$

By combining all the excitations in their respective order, the RHS can be expressed as a truncated Fourier series describing the complete forcing experienced by the system:

$$\mathbf{f}\left(\mathbf{x},\dot{\mathbf{x}},\ddot{\mathbf{x}},\omega,t\right)=\mathbf{f_0}+\sum_{k=1}^{m}\mathbf{f_k}e^{jk\omega t} \tag{2.4}$$

where $\mathbf{f_0}$ and $\mathbf{f_k}$ are arrays containing the Fourier coefficients of the forces. They are one-dimensional and their size is equal to the number of degrees of freedom of the system n. The number of kept harmonics m depends on the number of harmonics the nonlinear forces are expected to generate.

Since the above assumption is made for the excitation, the partial solution of the EOM must also have the same form, i.e. it is a periodic solution. Therefore:

$$\mathbf{x}\left(t\right)=\mathbf{x_0}+\sum_{k=1}^{m}\mathbf{x_k}e^{jk\omega t} \tag{2.5}$$

Differentiating Eq. 2.5 once for the velocity and twice for the acceleration and substituting in Eq. 2.2, the following holds:

$$\begin{aligned}\mathbf{M}\cdot\sum_{k=1}^{m}-\left(k\omega\right)^{2}\mathbf{x_k}e^{jk\omega t}+\mathbf{D}\cdot\sum_{k=1}^{m}jk\omega\mathbf{x_k}e^{jk\omega t}+&\\+\left(\mathbf{K}+j\mathbf{C}\right)\left(\mathbf{x_0}+\sum_{k=1}^{m}\mathbf{x_k}e^{jk\omega t}\right)&=\mathbf{f_0}+\sum_{k=1}^{m}\mathbf{f_k}e^{jk\omega t}\end{aligned} \tag{2.6}$$

The above equation is true if and only if:

$$\mathbf{K}\cdot\mathbf{x_0}=\mathbf{f_0} \tag{2.7}$$

and

$$\left(-\left(k\omega\right)^{2}\mathbf{M}+jk\omega\mathbf{D}+\mathbf{K}+j\mathbf{C}\right)\mathbf{x_k}=\mathbf{f_k},\quad\forall k\geq 1 \tag{2.8}$$

While mathematics dictates that eq. 2.7 should include the structural damping term, there is no structural damping when the system is in its static state.

Most numerical solvers cannot directly handle complex unknowns. This is why they must be decomposed into their real and imaginary parts. The coefficients of the zero harmonic only have a real part. Thus, $\mathbf{x_0} = \boldsymbol{\alpha}_\mathbf{0} + j\mathbf{0}$ and $\mathbf{x_k} = \boldsymbol{\alpha}_k + j\boldsymbol{\beta}_k$. Therefore, Eq. 2.7 and Eq. 2.8 can be written as follows:

$$\mathbf{K}\boldsymbol{\alpha}_\mathbf{0} + j\mathbf{0} = \mathbf{f_0} \tag{2.9}$$

and

$$-\left(k\omega\right)^2\mathbf{M}\boldsymbol{\alpha}_k + jk\omega\mathbf{D}\boldsymbol{\alpha}_k + \mathbf{K}\boldsymbol{\alpha}_k + j\mathbf{C}\boldsymbol{\alpha}_k - j\left(k\omega\right)^2\mathbf{M}\boldsymbol{\beta}_k - k\omega\mathbf{D}\boldsymbol{\beta}_k + j\mathbf{K}\boldsymbol{\beta}_k - \mathbf{C}\boldsymbol{\beta}_k = \mathbf{f_k} \tag{2.10}$$

To satisfy the above equations, the real and imaginary terms on both sides must be equal. This condition leads to the system of nonlinear equations for the classical harmonic balance method:

$$\begin{gathered}\mathbf{K}\boldsymbol{\alpha}_\mathbf{0} - \mathrm{Re}(\mathbf{f_0}) = \mathbf{0}\\ \left(\mathbf{K} - \left(k\omega\right)^2\mathbf{M}\right)\boldsymbol{\alpha}_k - \left(k\omega\mathbf{D} + \mathbf{C}\right)\boldsymbol{\beta}_k - \mathrm{Re}(\mathbf{f_k}) = \mathbf{0}\\ \left(\mathbf{K} - \left(k\omega\right)^2\mathbf{M}\right)\boldsymbol{\beta}_k + \left(k\omega\mathbf{D} + \mathbf{C}\right)\boldsymbol{\beta}_k - \mathrm{Im}(\mathbf{f_k}) = \mathbf{0}\end{gathered} \tag{2.11}$$

The unknowns in the classical harmonic balance method depend directly on the number of degrees of freedom n of the system and the number of kept harmonics m. For a simulation where the zero harmonic is included, the number of total equations is $(2 \cdot m + 1) \cdot n$, whereas if the zero harmonic is excluded, this number is reduced to $2 \cdot m \cdot n$.

2.3 Dynamic Condensation

In many applications, the nonlinear degrees of freedom are very low compared to the total degrees of freedom of the system. With the classical approach described in section 2.2, the entire system is solved as nonlinear, while the actual nonlinearity arises from only a few nodes. In this section, a dynamic condensation method is presented in order to greatly reduce the computational time by solving a nonlinear system of equations similar to the one described by Eq. 2.11, but only for the nonlinear degrees of freedom.

2.3.1 Partition of Equation of Motion

The first step is to perform a partition of the degrees of freedom into linear (p) and nonlinear (q). Mathematically, this is expressed as the linear transformation:

$$\mathbf{x} = \mathbf{P}\mathbf{y} = \mathbf{P}\left[\mathbf{y}^p \quad \mathbf{y}^q\right]^\top \tag{2.12}$$

where $\mathbf{P}$ is the partition matrix and $\mathbf{y}^p$, $\mathbf{y}^q$ are one-dimensional arrays containing the linear and nonlinear degrees of freedom respectively. Thus, Eq. 2.2 is written as follows:

$$\overbrace{\begin{bmatrix} \mathbf{M}_{pp} & \mathbf{M}_{pq} \\ \mathbf{M}_{qp} & \mathbf{M}_{qq} \end{bmatrix}}^{\tilde{\mathbf{M}}} \begin{bmatrix} \ddot{\mathbf{y}}^p \\ \ddot{\mathbf{y}}^q \end{bmatrix} + \overbrace{\begin{bmatrix} \mathbf{D}_{pp} & \mathbf{D}_{pq} \\ \mathbf{D}_{qp} & \mathbf{D}_{qq} \end{bmatrix}}^{\tilde{\mathbf{D}}} \begin{bmatrix} \dot{\mathbf{y}}^p \\ \dot{\mathbf{y}}^q \end{bmatrix} + \\ + \left(\underbrace{\begin{bmatrix} \mathbf{K}_{pp} & \mathbf{K}_{pq} \\ \mathbf{K}_{qp} & \mathbf{K}_{qq} \end{bmatrix}}_{\tilde{\mathbf{K}}} + \underbrace{\begin{bmatrix} \mathbf{C}_{pp} & \mathbf{C}_{pq} \\ \mathbf{C}_{qp} & \mathbf{C}_{qq} \end{bmatrix}}_{\tilde{\mathbf{C}}} \right) = \begin{bmatrix} \mathbf{f}^p \\ \mathbf{f}^q \end{bmatrix} \tag{2.13}$$

From Eq. 2.5 and Eq. 2.12 it is clear that the arrays $\mathbf{y}^p$, $\mathbf{y}^q$ can also be written as truncated Fourier series. Taking into consideration Eq. 2.4, the same applies for the arrays $\mathbf{f}^p$, $\mathbf{f}^q$. Therefore Eq. 2.13 is written as follows:

$$\tilde{\mathbf{M}} \begin{bmatrix} \sum_{k=1}^{m} - (k\omega)^2 \mathbf{y}_{\mathbf{k}}^p e^{jk\omega t} \\ \sum_{k=1}^{m} - (k\omega)^2 \mathbf{y}_{\mathbf{k}}^q e^{jk\omega t} \end{bmatrix} + \tilde{\mathbf{D}} \begin{bmatrix} \sum_{k=1}^{m} jk\omega \mathbf{y}_{\mathbf{k}}^p e^{jk\omega t} \\ \sum_{k=1}^{m} jk\omega \mathbf{y}_{\mathbf{k}}^q e^{jk\omega t} \end{bmatrix} + \\ + (\tilde{\mathbf{K}} + j\tilde{\mathbf{C}}) \begin{bmatrix} \mathbf{y}_0^p + \sum_{k=1}^{m} \mathbf{y}_{\mathbf{k}}^p e^{jk\omega t} \\ \mathbf{y}_0^q + \sum_{k=1}^{m} \mathbf{y}_{\mathbf{k}}^q e^{jk\omega t} \end{bmatrix} = \begin{bmatrix} \mathbf{f}_0^p + \sum_{k=1}^{m} \mathbf{f}_{\mathbf{k}}^p e^{jk\omega t} \\ \mathbf{f}_0^q + \sum_{k=1}^{m} \mathbf{f}_{\mathbf{k}}^q e^{jk\omega t} \end{bmatrix} \tag{2.14}$$

which is true under the following conditions (no structural damping provided in the static state):

$$\tilde{\mathbf{K}} \begin{bmatrix} \mathbf{y}_0^p \\ \mathbf{y}_0^q \end{bmatrix} = \begin{bmatrix} \mathbf{f}_0^p \\ \mathbf{f}_0^q \end{bmatrix} \tag{2.15}$$

and

$$\left(- (k\omega)^2 \tilde{\mathbf{M}} + jk\omega \tilde{\mathbf{D}} + \tilde{\mathbf{K}} + j\tilde{\mathbf{C}} \right) \begin{bmatrix} \mathbf{y}_{\mathbf{k}}^p \\ \mathbf{y}_{\mathbf{k}}^q \end{bmatrix} = \begin{bmatrix} \mathbf{f}_{\mathbf{k}}^p \\ \mathbf{f}_{\mathbf{k}}^q \end{bmatrix}, \quad \forall k \geq 1 \tag{2.16}$$

Equations 2.15 and 2.16 are the partitioned equivalents of Eq. 2.7 and Eq. 2.8, respectively.

2.3.2 Condensed equations for zero harmonic

In this section, the equations for the zero harmonic Fourier coefficients of the nonlinear degrees of freedom are derived. The complex unknowns of Eq. 2.15 are expressed as a real and an imaginary component. With the same procedure described in section 2.2, the following equation is obtained:

$$\begin{bmatrix} \mathbf{K}_{pp} & \mathbf{K}_{pq} \\ \mathbf{K}_{qp} & \mathbf{K}_{qq} \end{bmatrix} \begin{bmatrix} \boldsymbol{\alpha}_0^p \\ \boldsymbol{\alpha}_0^q \end{bmatrix} = \mathrm{Re} \begin{bmatrix} \mathbf{f}_0^p \\ \mathbf{f}_0^q \end{bmatrix} \tag{2.17}$$

From Eq. 2.17, two additional equations are yielded:

$$\mathbf{K}_{pp}\boldsymbol{\alpha}_0^p + \mathbf{K}_{pq}\boldsymbol{\alpha}_0^q = \mathrm{Re}(\mathbf{f}_0^p) \Leftrightarrow \boldsymbol{\alpha}_0^p = \mathbf{K}_{pp}^{-1} \cdot \left(\mathrm{Re}(\mathbf{f}_0^p) - \mathbf{K}_{pq}\boldsymbol{\alpha}_0^q\right) \tag{2.18}$$

$$\mathbf{K}_{qp}\boldsymbol{\alpha}_0^p + \mathbf{K}_{qq}\boldsymbol{\alpha}_0^q = \mathrm{Re}(\mathbf{f}_0^q) \tag{2.19}$$

By substituting Eq. 2.18 into Eq. 2.19, the unknown linear coefficients are eliminated and the equation for calculating the Fourier coefficients of the zero harmonic only for the nonlinear degrees of freedom is obtained:

$$\left(\mathbf{K}_{qq} - \mathbf{K}_{qp}\mathbf{K}_{pp}^{-1}\mathbf{K}_{pq}\right) \boldsymbol{\alpha}_0^q + \mathbf{K}_{qp}\mathbf{K}_{pp}^{-1}\,\mathrm{Re}(\mathbf{f}_0^p) - \mathrm{Re}(\mathbf{f}_0^q) = 0 \tag{2.20}$$

2.3.3 Condensed equations for higher harmonics - Real part

In this section, the equations for the real part of the k-harmonic Fourier coefficients of the nonlinear degrees of freedom are derived. For clarity reasons, the following symbols are introduced in Eq. 2.16:

$$\begin{bmatrix} \mathbf{y}_\mathbf{k}^p \\ \mathbf{y}_\mathbf{k}^q \end{bmatrix} = \begin{bmatrix} \boldsymbol{\alpha}_k^p \\ \boldsymbol{\alpha}_k^q \end{bmatrix} + j \begin{bmatrix} \boldsymbol{\beta}_k^p \\ \boldsymbol{\beta}_k^q \end{bmatrix} = \tilde{\boldsymbol{\alpha}}_k + j\tilde{\boldsymbol{\beta}}_k, \quad \begin{bmatrix} \mathbf{f}_\mathbf{k}^p \\ \mathbf{f}_\mathbf{k}^q \end{bmatrix} = \tilde{\mathbf{f}}_\mathbf{k} \tag{2.21}$$

Substituting these expressions in Eq. 2.16 and following the same procedure as in section 2.2, the following equations are obtained:

$$\left(\tilde{\mathbf{K}} - (k\omega)^2\,\tilde{\mathbf{M}}\right) \tilde{\boldsymbol{\alpha}}_k - \left(k\omega\tilde{\mathbf{D}} + \tilde{\mathbf{C}}\right) \tilde{\boldsymbol{\beta}}_k - \mathrm{Re}(\tilde{\mathbf{f}}_\mathbf{k}) = \mathbf{0} \tag{2.22}$$

$$\left(\tilde{\mathbf{K}} - (k\omega)^2\,\tilde{\mathbf{M}}\right) \tilde{\boldsymbol{\beta}}_k + \left(k\omega\tilde{\mathbf{D}} + \tilde{\mathbf{C}}\right) \tilde{\boldsymbol{\alpha}}_k - \mathrm{Im}(\tilde{\mathbf{f}}_\mathbf{k}) = \mathbf{0} \tag{2.23}$$

From Eq. 2.23:

$$\tilde{\boldsymbol{\beta}}_k = \left(\tilde{\mathbf{K}} - (k\omega)^2\,\tilde{\mathbf{M}}\right)^{-1} \mathrm{Im}(\tilde{\mathbf{f}}_\mathbf{k}) - \left(\tilde{\mathbf{K}} - (k\omega)^2\,\tilde{\mathbf{M}}\right)^{-1} \left(k\omega\tilde{\mathbf{D}} + \tilde{\mathbf{C}}\right)\tilde{\boldsymbol{\alpha}}_k \tag{2.24}$$

Substituting Eq. 2.24 into Eq. 2.22, the unknown $\tilde{\boldsymbol{\beta}}_k$ is eliminated and an equation containing only the real part of the Fourier coefficients is obtained:

$$\mathbf{T}_\mathbf{k}\tilde{\boldsymbol{\alpha}}_k = \mathbf{w}_\mathbf{k} \tag{2.25}$$

where:

$$\mathbf{T}_\mathbf{k} = \tilde{\mathbf{K}} - (k\omega)^2\,\tilde{\mathbf{M}} + \left(k\omega\tilde{\mathbf{D}} + \tilde{\mathbf{C}}\right)\left(\tilde{\mathbf{K}} - (k\omega)^2\,\tilde{\mathbf{M}}\right)^{-1}\left(k\omega\tilde{\mathbf{D}} + \tilde{\mathbf{C}}\right) \tag{2.26}$$

and

$$\mathbf{w}_\mathbf{k} = \mathrm{Re}(\tilde{\mathbf{f}}_\mathbf{k}) + \left(k\omega\tilde{\mathbf{D}} + \tilde{\mathbf{C}}\right)\left(\tilde{\mathbf{K}} - (k\omega)^2\,\tilde{\mathbf{M}}\right)^{-1}\mathrm{Im}(\tilde{\mathbf{f}}_\mathbf{k}) \tag{2.27}$$

Now, Eq. 2.25 can be expressed in its expanded form:

$$\begin{bmatrix} \mathbf{T}_{\mathbf{k},pp} & \mathbf{T}_{\mathbf{k},pq} \\ \mathbf{T}_{\mathbf{k},qp} & \mathbf{T}_{\mathbf{k},qq} \end{bmatrix} \begin{bmatrix} \boldsymbol{\alpha}_k^p \\ \boldsymbol{\alpha}_k^q \end{bmatrix} = \begin{bmatrix} \mathbf{w}_\mathbf{k}^p \\ \mathbf{w}_\mathbf{k}^q \end{bmatrix} \tag{2.28}$$

which is the same as Eq. 2.17. Therefore, using the same calculations performed to obtain Eq. 2.20, a similar expression is obtained for calculating the real part of the k-harmonic Fourier coefficients only for the nonlinear degrees of freedom:

$$\left(\mathbf{T}_{\mathbf{k},qq} - \mathbf{T}_{\mathbf{k},qp}\mathbf{T}_{\mathbf{k},pp}^{-1}\mathbf{T}_{\mathbf{k},pq}\right)\boldsymbol{\alpha}_k^q + \mathbf{T}_{\mathbf{k},qp}\mathbf{T}_{\mathbf{k},pp}^{-1}\mathbf{w}_\mathbf{k}^p - \mathbf{w}_\mathbf{k}^q = 0 \tag{2.29}$$

2.3.4 Condensed equations for higher harmonics - Imaginary part

In this section, the equations for the imaginary part of the k-harmonic Fourier coefficients of the nonlinear degrees of freedom are derived. The procedure is the same as the one followed in section 2.3.3. The difference lies in the variable that gets eliminated. From Eq. 2.22:

$$\tilde{\boldsymbol{\alpha}}_k = \left(\tilde{\mathbf{K}} - (k\omega)^2\,\tilde{\mathbf{M}}\right)^{-1}\left(k\omega\tilde{\mathbf{D}} + \tilde{\mathbf{C}}\right)\tilde{\boldsymbol{\beta}}_k + \left(\tilde{\mathbf{K}} - (k\omega)^2\,\tilde{\mathbf{M}}\right)^{-1}\mathrm{Re}(\tilde{\mathbf{f}}_\mathbf{k}) \tag{2.30}$$

Substituting Eq. 2.30 into Eq. 2.23, the unknown $\tilde{\boldsymbol{\alpha}}_k$ is eliminated and an equation containing only the imaginary part of the Fourier coefficients is obtained:

$$\mathbf{T_k}\tilde{\beta}_k = \mathbf{u_k} \tag{2.31}$$

where matrix $\mathbf{T_k}$ is calculated by Eq. 2.26 and $\mathbf{u_k}$ by:

$$\mathbf{u_k} = \mathrm{Im}(\tilde{\mathbf{f}}_\mathbf{k}) - \left(k\omega\tilde{\mathbf{D}} + \tilde{\mathbf{C}}\right)\left(\tilde{\mathbf{K}} - (k\omega)^2\tilde{\mathbf{M}}\right)^{-1}\mathrm{Re}(\tilde{\mathbf{f}}_\mathbf{k}) \tag{2.32}$$

As in the previous section, Eq. 2.31 can be expressed in its expanded form:

$$\begin{bmatrix} \mathbf{T}_{\mathbf{k},pp} & \mathbf{T}_{\mathbf{k},pq} \\ \mathbf{T}_{\mathbf{k},qp} & \mathbf{T}_{\mathbf{k},qq} \end{bmatrix} \begin{bmatrix} \beta_k^p \\ \beta_k^q \end{bmatrix} = \begin{bmatrix} \mathbf{u}_\mathbf{k}^p \\ \mathbf{u}_\mathbf{k}^q \end{bmatrix} \tag{2.33}$$

which is the same as Eq. 2.17. Therefore, using the same calculations performed to obtain Eq. 2.20, a similar expression is obtained for calculating the imaginary part of the k-harmonic Fourier coefficients only for the nonlinear degrees of freedom:

$$\left(\mathbf{T}_{\mathbf{k},qq} - \mathbf{T}_{\mathbf{k},qp}\mathbf{T}_{\mathbf{k},pp}^{-1}\mathbf{T}_{\mathbf{k},pq}\right)\beta_k^q + \mathbf{T}_{\mathbf{k},qp}\mathbf{T}_{\mathbf{k},pp}^{-1}\mathbf{u}_\mathbf{k}^p - \mathbf{u}_\mathbf{k}^q = 0 \tag{2.34}$$

With the equations for every harmonic obtained, the nonlinear system of equations for the harmonic balance method using a dynamic condensation approach is presented below:

$$\begin{aligned} \left(\mathbf{K}_{qq} - \mathbf{K}_{qp}\mathbf{K}_{pp}^{-1}\mathbf{K}_{pq}\right)\alpha_\mathbf{0}^q + \mathbf{K}_{qp}\mathbf{K}_{pp}^{-1}\mathrm{Re}(\mathbf{f}_\mathbf{0}^p) - \mathrm{Re}(\mathbf{f}_\mathbf{0}^q) = 0 \\ \left(\mathbf{T}_{\mathbf{k},qq} - \mathbf{T}_{\mathbf{k},qp}\mathbf{T}_{\mathbf{k},pp}^{-1}\mathbf{T}_{\mathbf{k},pq}\right)\alpha_k^q + \mathbf{T}_{\mathbf{k},qp}\mathbf{T}_{\mathbf{k},pp}^{-1}\mathbf{w}_\mathbf{k}^p - \mathbf{w}_\mathbf{k}^q = 0 \\ \left(\mathbf{T}_{\mathbf{k},qq} - \mathbf{T}_{\mathbf{k},qp}\mathbf{T}_{\mathbf{k},pp}^{-1}\mathbf{T}_{\mathbf{k},pq}\right)\beta_k^q + \mathbf{T}_{\mathbf{k},qp}\mathbf{T}_{\mathbf{k},pp}^{-1}\mathbf{u}_\mathbf{k}^p - \mathbf{u}_\mathbf{k}^q = 0 \end{aligned} \tag{2.35}$$

This system is the condensed equivalent of the system described by Eq. 2.11. The reader will notice that the number of equations to solve now depends on the number of kept harmonics m and the number of nonlinear degrees of freedom q, instead of the number of total degrees of freedom n. This is a significant improvement in terms of efficiency, since the systems studied in this thesis contain hundreds of degrees of freedom, but only a few nonlinear ones. An example of a system with $n = 500$, $q = 8$ and 2 harmonics (0x, 1x) shows that using the classical harmonic balancing method the nonlinear equations are 1500, while using dynamic condensation the equations are reduced to 24.

After solving Eq. 2.35, the Fourier coefficients of the linear degrees of freedom can be estimated by Eq. 2.18, 2.28, 2.33. More specifically, a linear system can be solved to obtain every linear unknown:

$$\begin{aligned} \mathbf{K}_{pp}\alpha_\mathbf{0}^p &= \mathrm{Re}(\mathbf{f}_\mathbf{0}^p) - \mathbf{K}_{pq}\alpha_\mathbf{0}^q \\ \mathbf{T}_{\mathbf{k},pp}\alpha_k^p &= \mathbf{w}_\mathbf{k}^p - \mathbf{T}_{\mathbf{k},pq}\alpha_k^q \\ \mathbf{T}_{\mathbf{k},pp}\beta_k^p &= \mathbf{u}_\mathbf{k}^p - \mathbf{T}_{\mathbf{k},pq}\beta_k^q \end{aligned} \tag{2.36}$$

2.4 Solution algorithm

This section presents the solution procedure for the nonlinear condensed system described by Eq. 2.35. The unknowns are the arrays $\boldsymbol{\alpha}_0^q$, $\boldsymbol{\alpha}_k^q$, $\boldsymbol{\beta}_k^q$. Each array contains q coefficients, as many as there are nonlinear degrees of freedom. These values are organized into a single one-dimensional array of unknowns $\mathbf{r}$ for handling by the numerical solver. The general format of this array is shown below:

$$\mathbf{r} = [\, \underbrace{\boldsymbol{\alpha}_1^q\ \boldsymbol{\alpha}_2^q\ \dots\ \boldsymbol{\alpha}_m^q}_{m\cdot q}\ \underbrace{\boldsymbol{\beta}_1^q\ \boldsymbol{\beta}_2^q\ \dots\ \boldsymbol{\beta}_m^q}_{m\cdot q}\ \underbrace{\boldsymbol{\alpha}_0^q}_{q}\,] \tag{2.37}$$

where the subscripts $0, 1, \dots, m$ denote the harmonic. With the introduction of this variable, the nonlinear system of Eq. 2.35 can be expressed mathematically in one line as follows:

$$G(\mathbf{r}) = 0 \tag{2.38}$$

2.4.1 Calculation of the nonlinear force coefficients

An important part of the solution procedure is the calculation of the nonlinear force Fourier coefficients. These coefficients are also stored in a one-dimensional array, the general format of which is shown below:

$$\mathbf{f_{NL}} = \left[\underbrace{\mathbf{f}_{\mathbf{1,NL}}^q\ \mathbf{f}_{\mathbf{2,NL}}^q\ \dots\ \mathbf{f}_{\mathbf{m,NL}}^q}_{m\cdot q}\ \underbrace{\mathbf{f}_{\mathbf{0,NL}}^q}_{q} \right] \tag{2.39}$$

where again the subscripts $0, 1, \dots, m$ denote the harmonic. Similar to array $\mathbf{r}$, each individual force array contains q coefficients. The difference is that compared to array $\mathbf{r}$, the coefficients in array $\mathbf{f_{NL}}$ are kept in their complex form. Calculating them directly in the frequency domain would be a complex task due to the nature of the nonlinearities. Therefore, the Alternate Frequency-Time domain (AFT) method proposed by Cameron and Griffin [11] is used for their calculation.

$$\mathbf{r} \xrightarrow{FFT^{-1}} \mathbf{x}(t) \longrightarrow \mathbf{f_{NL}}(\mathbf{x}, \dot{\mathbf{x}}, \ddot{\mathbf{x}}, \omega, t) \xrightarrow{FFT} \mathbf{f_{NL}}$$

Figure 2.1: Schematic description of the AFT-method.

Essentially, the vector in Eq. 2.37 describes the motion of the system in the frequency domain. Using an inverse FFT, this motion can be translated to the time domain, where the nonlinear reaction forces from the SFD and/or REB are then calculated. Finally, the force coefficients in the frequency domain are obtained by applying an FFT directly to the force signal.

To obtain the correct force arrays present in Eq. 2.35, the weight and unbalance force array $\mathbf{f_g}$ and $\mathbf{f_u}$ must be partitioned. Hence, the arrays $\mathbf{f_g^p}$, $\mathbf{f_g^q}$, $\mathbf{f_u^p}$ and $\mathbf{f_u^q}$ are obtained. As mentioned at the beginning of section 2.2, the weight force corresponds to a zero order excitation and the unbalance force to a first order excitation. Therefore, the following relations hold for the total excitation of zero, first $(k = 1)$ and higher harmonics $(k = 2 \ldots m)$:

Table 2.1: Relations for the total excitation force arrays depending on the harmonic

$k = 0$	$k = 1$	$k \geq 2$
$\mathbf{f_0^p} = \mathbf{f_g^p}$	$\mathbf{f_1^p} = \mathbf{f_u^p}$	$\mathbf{f_k^p} = \mathbf{0}$
$\mathbf{f_0^q} = \mathbf{f_g^q} + \mathbf{f_{0,NL}^q}$	$\mathbf{f_1^q} = \mathbf{f_u^q} + \mathbf{f_{1,NL}^q}$	$\mathbf{f_k^q} = \mathbf{f_{k,NL}^q}$

These equations allow for the calculation of the arrays $\mathbf{f_0^p}$, $\mathbf{f_0^q}$, $\mathbf{w_k^p}$, $\mathbf{w_k^q}$, $\mathbf{u_k^p}$ and $\mathbf{u_k^q}$ which are all present in the condensed system of 2.35.

2.4.2 Solution algorithm schematic

The procedure for solving the condensed Harmonic Balance system of equations described by Eq. 2.35 is shown in Fig. 2.2. The dark-colored boxes represent the AFT-method described in the previous section. To start the simulation, the user must specify among other inputs, the location of the nonlinear elements (nodes of the system) and the model used to calculate the reaction forces. These models can be analytical or numerical and they will be discussed in later chapters. In addition, the harmonics to be included in the simulation must be specified.

The AFT parameters are also user-defined. They consist of the number of sample points and the number of sample periods used in the FFT. The latter is always equal to one, unless multiple frequency excitations occur. This case is discussed in the next section. The number of sample points P greatly influences the efficiency of the algorithm and thus extra care must be taken when choosing this value. For up to the third harmonic, $P = 8$ is sufficient. For additional harmonics, 16 points are recommended. In general, since an FFT algorithm is used, this number must obey the following relation:

$$P \geq 2^m \tag{2.40}$$

where m is the number of kept harmonics, excluding the zero harmonic.

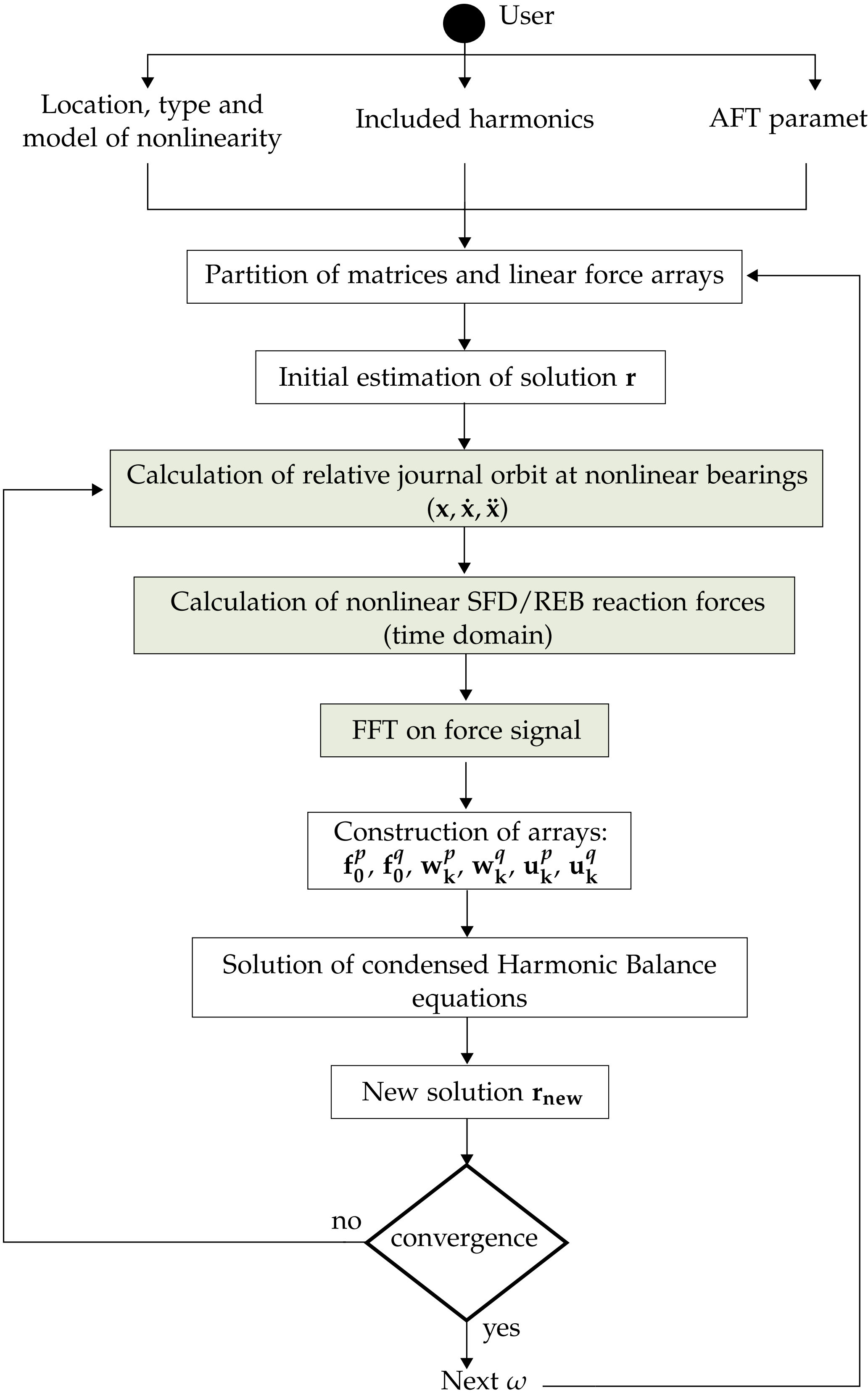

Figure 2.2: Schematic representation of the solution procedure for the nonlinear, condensed system of equations.

After selecting these parameters, the linear and nonlinear degrees of freedom are separated and the solution for the first frequency begins. The process is iterative because the system of 2.35 is nonlinear. As with all nonlinear systems, an initial solution is required, which is obtained from the three previously converged solutions using Lagrange polynomials for equidistant solution steps. Then, the AFT method described in the previous section is applied. From the resulting force coefficients, the function G of Eq. 2.38 can be calculated at $\mathbf{r}$ along with its derivative and then a new solution can be estimated. This procedure is repeated until convergence, at which point the user can choose to calculate the coefficients for the linear degrees of freedom as well. The algorithm proceeds to the next frequency step and the process is repeated until convergence.

The algorithm described above can also be run in parallel if the user so chooses. This is particularly useful when the numerical nonlinear models, which are described in more detail in Chapter 3, are being used. Since these models are slower than an analytical expression, running the simulation in parallel greatly reduces the simulation cost. In addition, parallelization is often used in this work when the number of harmonics increases, since the equations approximately double along with the simulation time. The frequency range can be divided into as many cores as are available, and each subrange can be run on a separate thread. However, care must be taken when selecting the subranges to not start on a resonance peak. Since the initial solution there won't have the information of the previous solutions, the solver may not converge. To avoid this behavior, a linear analysis can be performed a priori to get a good understanding of where the resonance peaks are located.

The exact algorithm used to solve the nonlinear system is a modification of the Powell hybrid method. In this algorithm, the Jacobian is approximated using finite differences. This routine is part of the algorithms of MINPACK. Since the programming language used in this work is Python, the routine is accessed through the scipy library [49]. For the parallelization, the multiprocessing library is used.

2.5 Multiple frequency excitation

In the simple case of a single frequency excitation, the force acting on the system can be expressed according to Eq. 2.4. The frequency ω is the base or reference frequency, which in this work corresponds to the rotational speed of the unbalance rotor. When performing the AFT steps, only one sampling period $T = 2\pi/\omega$ is required to obtain the correct result, since the time signal is periodic in this period. As discussed in paragraph 2.4.2, the number of sampling points P is adjusted according to the number of kept harmonics.

In this work, the case of multiple unbalanced rotors is also considered. Now, besides the reference frequency ω, there is a secondary excitation frequency ω_{sec}, which arises from an unbalance located on another rotor, called the secondary rotor. The secondary frequency is related to the reference frequency by the speed ratio (sr), so $\omega_{sec} = sr \cdot \omega$. Each of these frequencies has its corresponding harmonics. The time signal calculated in the first step of the AFT now has the information on both frequencies. If the sampling period is kept to one, then the resulting time signal will contain the full reference signal, but the secondary signal will be truncated, resulting in a quasi-periodic solution.

Since the harmonic balance method presented in this work cannot directly handle quasi-periodic solutions, a different approach is considered. By restricting the speed ratio to only commensurable frequencies, a number of sampling periods are selected that completely encompass both the reference and secondary signals. In the case of a speed ratio $sr = 1.5$, the procedure is illustrated in Fig. 2.3 for the 1x (reference) and 1.5x (secondary) components. The AFT now requires two sample periods and twice as many sample points P. Therefore, there will be 2 reference signals and 3 secondary signals in the final time signal. There will be no truncation occurring, so the resulting signal will be periodic and the harmonic balance method can be applied as is.

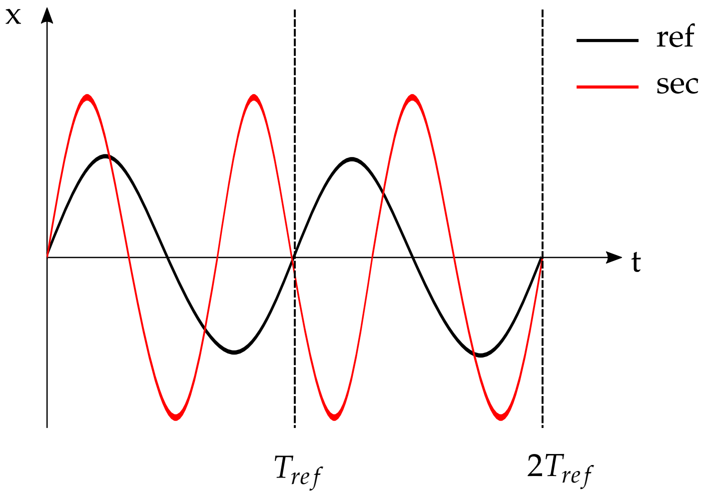

Figure 2.3: Visual representation of the extension of the sampling period in order to keep the solution periodic in the case of a dual unbalance excitation.

3 Nonlinear Element Models

3.1 Squeeze Film Damper Modeling

3.1.1 Short Bearing Modeling

The short bearing model provides analytical expressions for the reaction forces of an SFD. It is the simplest model available and one of the most commonly used in rotor dynamic simulations due to its efficiency and ease of integration. The model is derived from the Reynolds equation, which in turn is derived from the Navier-Stokes equations in conjunction with the continuity equation.

The Navier-Stokes equations describe the motion of a Newtonian fluid and are an expression of the conservation of momentum in a fluid volume. For an incompressible fluid with constant dynamic viscosity η, they can be expressed concisely as [53]

$$\rho \frac{\partial \mathbf{u}}{\partial t} + \rho \mathbf{u} \left(\nabla \cdot \mathbf{u} \right) = -\nabla p + \eta \nabla^2 \mathbf{u} + \rho \mathbf{g} \tag{3.1}$$

where $\mathbf{u}$ is a vector containing the velocity components of the fluid in all three directions and p is the pressure. The first and second terms on the left-hand side of Eq. 3.1 represent the temporal and convective inertia, respectively. To simplify the equations, certain assumptions are made. The inertia terms are neglected and the velocity in the direction of the gap is assumed to be zero due to the small size of the film thickness. Additionally, the gravitational terms are neglected and the pressure across the gap is assumed to be constant. With these simplifications and the use of the continuity equation, the Reynolds equation is derived and expressed in cylindrical coordinates for an SFD [4],

$$\frac{\partial}{R\partial\theta} \left(\frac{\rho h^3}{12\eta} \cdot \frac{\partial p}{R\partial\theta} \right) + \frac{\partial}{\partial z} \left(\frac{\rho h^3}{12\eta} \cdot \frac{\partial p}{\partial z} \right) = \frac{\partial \left(\rho h \right)}{\partial t} \tag{3.2}$$

where θ is the circumferential direction, z is the axial direction, η is the dynamic viscosity of the fluid and h is the oil film thickness. A more detailed presentation for the derivation of the Reynolds equation can be found in [44] and [5]. The short bearing assumption further simplifies Eq. 3.2 by assuming that due to the short length, the pressure gradient in the axial z-direction is significantly larger than in the x-direction. Therefore, the corresponding term on the left hand side is neglected and the resulting equation yields an analytical solution for the pressure field [44].

$$P(\theta, z) = \frac{6\eta}{h^3} \cdot [-\dot{x} \cdot \cos\theta - \dot{y} \cdot \sin\theta] \cdot (z^2 - L \cdot z) \tag{3.3}$$

To calculate the reaction forces in the x and y directions, the following integrations are performed,

$$\begin{aligned} F_x &= \int_0^L \int_0^{2\pi} P(\theta, z) \cdot \cos\theta \cdot R \, d\theta \, dz \\ F_y &= \int_0^L \int_0^{2\pi} P(\theta, z) \cdot \sin\theta \cdot R \, d\theta \, dz \end{aligned} \tag{3.4}$$

where L is the length of the SFD and R is its radius. The analytical expressions for the reaction forces in the x and y directions can now be obtained,

$$\begin{aligned} F_x &= \eta \cdot R \cdot L^3 \int_0^{2\pi} \frac{\dot{x} \cdot \cos^2\theta + \dot{y} \cdot \sin\theta \cdot \cos\theta}{(c_r - x \cdot \cos\theta - y \cdot \sin\theta)^3} \, d\theta \\ F_y &= \eta \cdot R \cdot L^3 \int_0^{2\pi} \frac{\dot{x} \cdot \cos\theta \cdot \sin\theta + \dot{y} \cdot \sin^2\theta}{(c_r - x \cdot \cos\theta - y \cdot \sin\theta)^3} \, d\theta \end{aligned} \tag{3.5}$$

where the integral that remains can be calculated numerically.

3.1.2 State-of-the-Art Modeling

In many practical applications, the simple short bearing approach is not sufficient to adequately capture the complex geometric and operational features present in a squeeze film damper. Therefore, more detailed models have been developed. The main difference from the short bearing model is that the Reynolds equation is now discretized and solved numerically. This approach is called the finite bearing model. In this section, the most recent models available for the calculation of SFD reaction forces are briefly presented. The objective of this work is not to delve into the SFD modeling, but rather to integrate certain state-of-the-art models into the harmonic balance simulations and to interpret the results.

The section is divided into two parts, the isothermal modeling, where the temperature of the lubricant is kept constant, and the thermal modeling, where the temperature inside the damper is allowed to vary.

Isothermal Modeling in Squeeze Film Dampers

When the temperature of the fluid is held constant, the viscosity of the fluid remains the same and the Reynolds equation of 3.2 is solved as is.

The finite element approach allows complex geometric features to be modeled. An important feature found in many squeeze film dampers is a circumferential groove. The primary function of the groove is to provide a continuous supply of oil to the damper surfaces, commonly referred to as lands. When modeling a circumferential groove, the effects of inertia can become important. In the work of San Andres [6], the temporal inertia term is included, resulting in the modified Reynolds equation [4].

$$\frac{\partial}{R\partial\theta}\left(\frac{\rho h^3}{12\eta}\cdot\frac{\partial p}{R\partial\theta}\right)+\frac{\partial}{\partial z}\left(\frac{\rho h^3}{12\eta}\cdot\frac{\partial p}{\partial z}\right)=\frac{\partial\left(\rho h\right)}{\partial t}+\frac{\rho h^2}{12\eta}\cdot\frac{\partial^2\left(\rho h\right)}{\partial t^2} \tag{3.6}$$

For low eccentricity amplitude motions of the journal within the SFD, the temporal inertia term is assumed to be much larger than the convective term [18]. For this reason, the state-of-the-art temporal inertia model [6] should be limited to such motions. In the work of Hamzehlouia [29, 27], the convective term is also considered and thus a complete modeling of the inertial effects is achieved.

In the work of Gheller et al. [22], the authors mention another important feature in SFDs, called the piston ring seal. They explain that when the SFD has an open-ends configuration, the lubricant is directly exposed to the ambient pressure and is therefore subject to significant air entrainment, which reduces damping capability. This is the reason piston ring seals are used, which are placed in corresponding piston ring grooves on both sides of the SFD. Their presence is imposed as an outlet boundary condition and is modeled as a restriction on the outlet flow rate of the lubricant,

$$q_{out}=\frac{C_p\left(P\left(\theta,L\right)-P_{out}\right)h_p^3}{12\eta w_p} \tag{3.7}$$

where C_p is the piston ring loss coefficient, P_{out} is the pressure on the outer side of the piston ring and h_p, w_p describe the geometry and position of the piston ring groove, respectively. Imposing all necessary inlet and outlet boundary conditions as well as other geometrical features present in the SFD, the Reynolds equation is solved and the reaction forces are calculated using Eq. 3.4.

Thermal Modeling in Squeeze Film Dampers

In thermal modeling, the temperature of the lubricant, and thus its viscosity, varies inside the damper. To account for this effect, the Reynolds equation of Dowson is used [15]

$$\frac{\partial}{\partial x_i}\left(\rho G\frac{\partial p}{\partial x_j}\right)=u_{journal,i}\frac{\partial\left(\rho F\right)}{\partial x_i}+\frac{\partial\left(\rho h\right)}{\partial t} \tag{3.8}$$

where $G = J_4 - J_1^2/J_0$ and $F = J_1/J_0$. The Dowson integrals J_0, J_1, J_4 represent the variation of the viscosity in regards to the gap height and are described by the following expressions

$$J_0 = \int_0^h \frac{1}{\eta\left(T\right)} dz, \quad J_1 = \int_0^h \frac{z}{\eta\left(T\right)} dz, \quad J_4 = \int_0^h \frac{z^2}{\eta\left(T\right)} dz \tag{3.9}$$

where z represents the gap height coordinate and h is the total oil film gap. The variation of the viscosity with temperature $\eta\left(T\right)$ is given by the Vogels equation

$$\eta\left(T\right) = c_1 e^{\left(\frac{c_2}{T+c_3}\right)} \tag{3.10}$$

where c_1, c_2, c_3 are Vogel parameters. The temperature distribution of the lubricant across the gap height z is a parabolic curve described in [50, 33]. For its calculation, the average temperature of the fluid across the gap height $\overline{T}$ must also be calculated. This is done by the 3D energy equation for fluid in tribological contact [36], which, integrated across the gap height, has the following 2D form

$$h\overline{\rho c}_p \left(\overline{U}\frac{\partial \overline{T}}{\partial x} + \overline{V}\frac{\partial \overline{T}}{\partial y}\right) - \frac{\partial}{\partial x}\left(h\overline{\lambda}\frac{\partial \overline{T}}{\partial x}\right) - \frac{\partial}{\partial y}\left(h\overline{\lambda}\frac{\partial \overline{T}}{\partial y}\right) - \overline{\lambda}\left[\frac{\partial \overline{T}}{\partial z}\right]_0^h = \overline{\Phi}_{hyd} \tag{3.11}$$

The temperature of the fluid is also affected by the temperature of the journal and the housing and vice versa. The energy equation for the solids is given by

$$\rho c_p \frac{\partial T}{\partial t} - \frac{\partial}{\partial x}\left(\lambda\frac{\partial T}{\partial x}\right) - \frac{\partial}{\partial y}\left(\lambda\frac{\partial T}{\partial y}\right) - \frac{\partial}{\partial z}\left(\lambda\frac{\partial T}{\partial z}\right) = \dot{q} \tag{3.12}$$

Therefore the complete thermal modeling contains three equations that need to be solved, Eq. 3.8, Eq. 3.11 and Eq. 3.12. These equations are nonlinear, time-dependent partial differential equations (PDEs) and they are solved simultaneously since they are coupled with one another. It is also possible to solve only the fluid energy equation and neglect the solid energy equation if boundary conditions are imposed for the journal and housing temperatures.

3.2 Rolling Element Bearing Modeling

Rolling element bearing models can be divided into kinematic and dynamic models based on the effects they consider. In this work, the effect of the first category is studied by integrating the standard kinematic model and the elastohydrodynamic model developed for ball bearings in the work of Stylianopoulou [57]. In order to couple the models with the motion of the shaft at different rotational speeds, it is assumed that the inner rings follow exactly the displacement of the shaft. Although this assumption differs from reality due to the fit between the two bodies, the difference is negligible. Finally, for the correct coupling of the model, the bearing must be preloaded in the axial direction to avoid free-play.

Standard Kinematic Model

The standard kinematic model is based on the kinematic and geometric relationships proposed by Lim and Singh [41]. It includes certain simplifying assumptions, such as keeping the angle between two balls constant, treating the cages as rigid bodies, including pin retainers, and neglecting centrifugal or gyroscopic effects. In addition, thermal effects are not considered. The key point in this model is that the rolling elements are in dry contact with the inner and outer rings and therefore a Hertzian parameter must be calculated in order to calculate the forces.

As the inner ring displaces, the elastic force exerted by each ball k can be calculated using the following expression,

$$Q_{n,k} = K_H \cdot \delta_k^{\frac{3}{2}} \tag{3.13}$$

where K_H is the Hertzian parameter and δ_k is the elastic deformation of the ball. The exponent value is one typically used in ball bearing calculations. The normal force calculated by Eq. 3.13 must then be projected to the global inner ring coordinate system using the Lim and Singh projection vector of each ball and then the contribution of the total number of balls N must be added together. The resulting force vector is given by

$$\mathbf{f} = \sum_{k=1}^{N} Q_{n,k} \cdot \mathbf{e}_{f_{LS},k} \tag{3.14}$$

where

$$\mathbf{f} = \begin{pmatrix} F_x & F_y & F_z & M_x & M_y & M_z \end{pmatrix} \tag{3.15}$$

Elastohydrodynamic Model

The main difference between the elastohydrodynamic (EHD) model and the standard kinematic model is the presence of a lubricant film between the rolling elements and the inner/outer ring. In addition to reducing wear, the lubricant also introduces viscous damping into the system. In addition, at high speeds and load conditions, it further increases the elastic deformation of the ball compared to dry contact only. This effect is described by

$$\delta_k = \delta_{H,k} - \delta_{EHD,k} \tag{3.16}$$

where δ_k is the total elastic deformation of the ball, $\delta_{EHD,k}$ is the elastic deformation due to the elastohydrodynamic effect and $\delta_{H,k}$ is the elastic deformation due to the dry contact. It can be shown that Eq. 3.16 can be expressed as [65, 57]

$$\delta_k = \left(\frac{Q_{n,k}}{K_{H,in}}\right)^{\frac{2}{3}} \left[1 - p_{in}\left(N_{red,in} Q_{n,k}\right)^{q_{in}}\right] + \left(\frac{Q_{n,k}}{K_{H,out}}\right)^{\frac{2}{3}} \left[1 - p_{out}\left(N_{red,out} Q_{n,k}\right)^{q_{out}}\right] \tag{3.17}$$

where $Q_{n,k}$ is the normal elastic force that is exerted from ball k, p and q are bearing parameters and N_{red} is a dimensionless load parameter. The subscripts *in* and *out* refer to the inner and outer rings, respectively. Eq. 3.17 is solved using an iterative procedure to calculate $Q_{n,k}$. After obtaining the elastic normal force of the ball, a dimensional damping coefficient c can be calculated for both ball-inner and ball-outer ring contacts. The total damping coefficient is given by

$$c_{tot} = \frac{1}{\frac{1}{c_{in}} + \frac{1}{c_{out}}} \tag{3.18}$$

from which the damping force exerted by the ball can be calculated according to

$$Q_{d,k} = \dot{\delta}_k c_{tot} \tag{3.19}$$

where the calculation of $\dot{\delta}_k$ is also given in the literature [57]. Similar to the standard kinematic model, the reaction force of each ball is projected onto the global inner ring coordinate system using the projection vector proposed by Wagner [63].

$$\mathbf{f} = \sum_{k=1}^{N} \left(Q_{n,k} + Q_{d,k}\right) \cdot \mathbf{e}_{f,k} \tag{3.20}$$

Note that there is no geometric difference between the Wagner projection vector and the Lim and Singh projection vector. The latter is expressed for use in specific analytical formulas for calculating the stiffness matrix, while the former is a more general expression.

4 Generic Jet Engine Dynamic Simulations

4.1 Jet Engine Model

The simulation results presented in this chapter revolve around the model displayed in Fig. 4.1. The model is a generic representation of a dual-spool jet engine, consisting of a Low Pressure (LP) and a High Pressure (HP) rotor, an outer casing and various bearing casing structures. Both rotors are hollow and they can rotate in the same direction (co-rotating) or in the opposite (contra-rotating). In this work, the rotors are contra-rotating, with the HP rotor rotating 1.5 times faster than the LP rotor. At the front of the LP and HP rotors are the LP compressor (LPC) and the HP compressor (HPC), respectively. The former has three stages, while the latter has five. At the rear of the rotors are the LP turbine (LPT) and the HP turbine (HPT), each with one stage.

Bearings and connecting structures are represented as springs. These springs can be either linear or nonlinear. Springs SP1 through SP3 represent struts, used to connect the bearing housings to the outer casing. Springs M1 and M2 have one end connected to the ground, hence they are not directly visible in the figure. They are used to represent the mounts used to connect the engine to the airframe. Springs B1 through B5 depicts the location of the rolling element bearings (REBs). The location of the SFD is shown with the corresponding spring.

The rotors and casings are modeled using Timoshenko beam elements, while the stages are represented as rigid disks with specific masses and moments of inertia since their geometric complexity is of little value for rotor dynamic simulations. It is worth noting that the structure OR is considered a casing since it does not rotate, but in reality, it represents the outer ring of a REB. In the detailed view of Fig. 4.1, the SQC element represents the squirrel cage used to centralize the SFD. Its complex geometry is best represented using the flexibility matrix approach presented in [10]. The left end of the SQC is rigidly connected to the casing above it.

In this model, the nonlinear elements can be either the SFD spring and/or one of the B1-B5 springs. In the present work, the SFD and B3 springs are treated as nonlinear to understand their effects on the dynamics. The models presented in Chapter 3 are used to calculate their reaction forces. Since the model in Fig. 4.1 represents a whole engine, it will be referred to as a Whole Engine Model (WEM).

4.2 Critical Speed Analysis

The first step in a rotor dynamic analysis is to calculate the critical speeds of the system. In addition to information about the motion of the system, the engineer can predict if

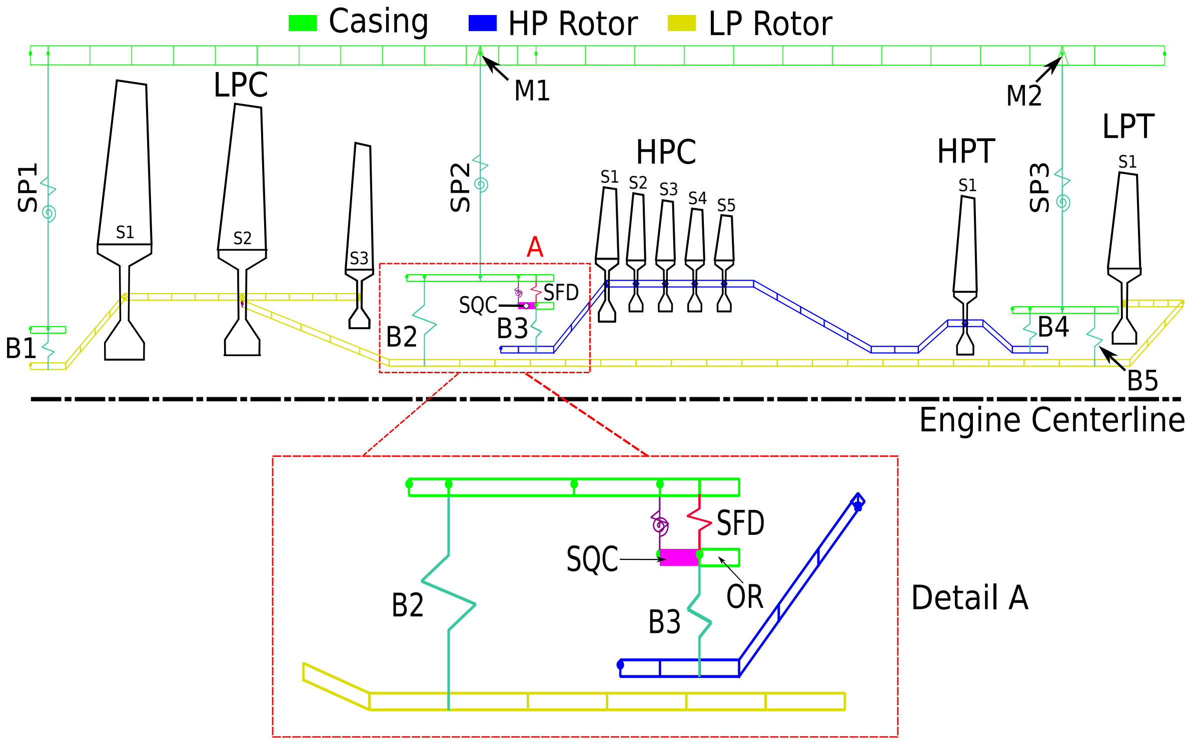

Figure 4.1: Generic jet engine model (MTU in-house tool).

and where an SFD will be of value and what peaks to expect in a frequency response analysis.

To calculate the critical speeds and corresponding modes, the eigenvalue problem must first be solved for discrete speeds of a given reference rotor. In the dual-spool system presented in this chapter, the LP rotor acts as the reference. By calculating the eigenvalues for each speed, the natural undamped frequencies are obtained and the results are displayed in a single figure called Campbell diagram. Fig. 4.2 shows this diagram for the case of contra-rotating rotors with a speed ratio of $\omega_{HP}/\omega_{LP} = -1.5$.

The black line represents the unbalance excitation frequency due to the reference rotor, which is the LP, while the magenta line represents the unbalance excitation frequency due to the secondary rotor, which is the HP. The points of intersection of these lines with the Campbell diagram are the critical speeds of the system. These values correspond to a forward (FW) or backward (BW) system mode. Whether the mode is FW or BW depends on the choice of reference rotor.

In this specific case, the LP rotor can only excite FW modes because its unbalance rotates in the same direction as it. In contrast, the HP rotor can only excite BW modes since its unbalance rotates in the opposite direction relative to the reference rotor. The critical speeds for this case are shown in Table 4.1. The letter L indicates the presence of a critical speed due to the unbalance on the LP rotor, while the letter H indicates the presence of a critical speed due to the unbalance on the HP rotor. Therefore, depending on which rotor the unbalance is on, peaks at these speeds can be expected in a frequency response analysis. The maximum speed of the LP rotor is 18000 rpm, so the critical speeds shown are limited by this value.

As mentioned earlier, one of the main reasons for performing a critical speed analysis is to gain an initial understanding of whether the installation of an SFD will benefit the

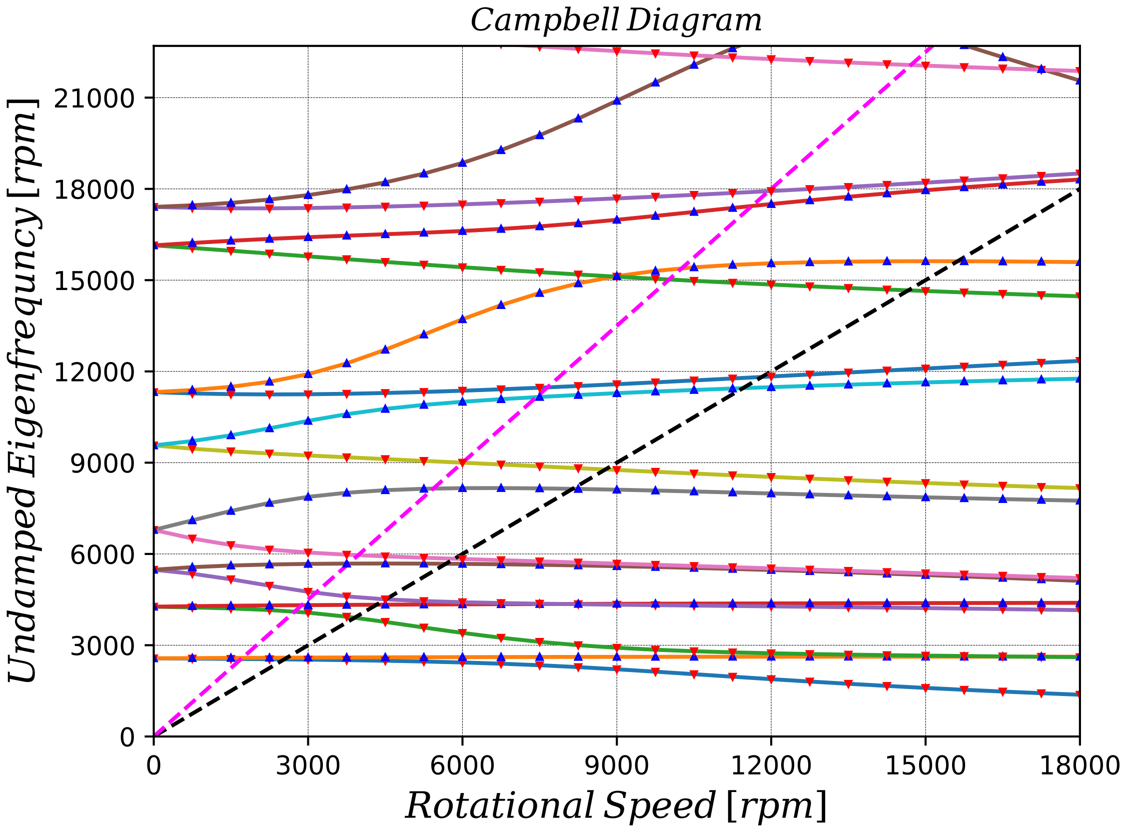

Figure 4.2: Campbell diagram for the case of contra-rotating rotors with LP rotor as reference.

system. An appropriate metric for this case is the squirrel cage (SQC) potential energy relative to the total system potential energy. A high value of this metric indicates that there is significant movement of the journal within the SFD, and thus the corresponding modes are sensitive to the damping provided by it. From Table 4.1, it is possible to predict that the modes L3, L5 and H4, H6 will be the most affected by the SFD damping. This prediction is further supported in the following section. In both cases, the LP rotor speed is the reference.

4.3 Linear Harmonic Analysis

The second step in a rotor dynamic analysis and a major factor in deciding for or against a SFD is to perform a linear harmonic analysis to observe if the resonances predicted by the Campbell diagram are indeed sensitive to the damping provided by a SFD. The analysis is performed for different damping coefficient values for the SFD spring, with the term ”linear” denoting that the damping force of the spring is expressed as $\mathbf{C_{SFD}} \cdot \dot{\mathbf{x}}$, where $\mathbf{C_{SFD}}$ is the damping matrix of the SFD, containing the damping coefficients. These are assumed isotropic and constant throughout the simulation, with no cross-coupling present.

Table 4.1: Critical speeds and potential energy distribution at the SQC element for the case of contra-rotating rotors

Critical speed (rpm)	Name	SQC Potential Energy (%)
1698	H1	0.02%
2590	L1	0.08%
2734	H2	1.09%
3146	H3	0.01%
3967	H4	**12.2%**
4329	L2	0.9%
5672	L3	**23.1%**
5985	H5	0.02%
7633	H6	**36.3%**
8126	L4	1.1%
9949	H7	0.4%
11416	L5	**30.9%**
11901	H8	1.94%
14606	H9	0.9%
15556	L6	0.4%

Two different unbalance scenarios are investigated. The first one, depicted in Fig. 4.3, represents the case where a single unbalance of 100 gmm is placed on the first stage of the HP compressor (HPC-S1). The second case, depicted in Fig. 4.4, represents the scenario where two unbalances of magnitude 100 gmm each and zero phase difference are placed on the first compressor and turbine stage of the LP rotor (LPC-S1 and LPT-S1).

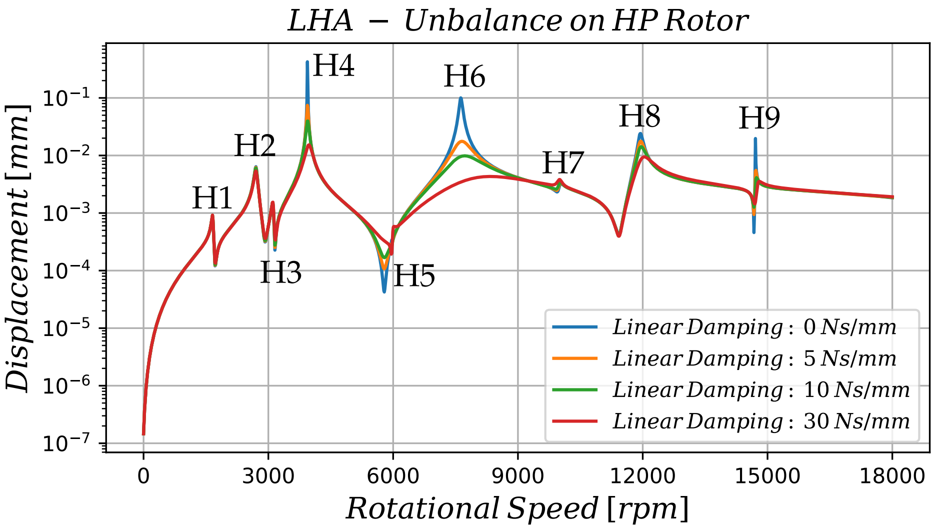

Figure 4.3: Linear frequency response of HPC-S1 for varying SFD spring damping values with the unbalance located on the HPC-S1.

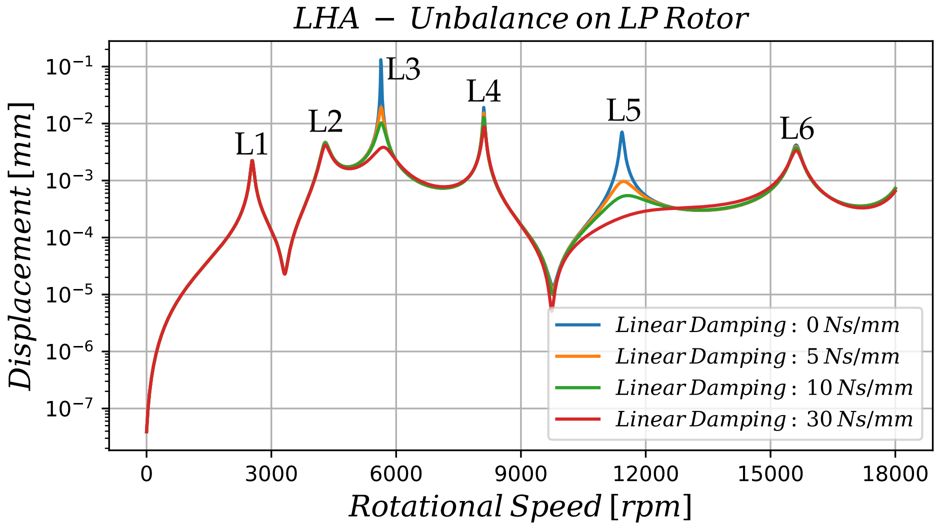

Figure 4.4: Linear frequency response of HPC-S1 for varying SFD spring damping values with the unbalance located on the LPC-S1 and LPT-S1.

It is clear that the SFD damping has a strong effect in attenuating the resonances of H4, H6 and L3, L5 as predicted from Table 4.1. Therefore, the SFD is of value to the system and further investigation of its effects and design is justified.

4.4 Nonlinear Simulations using the Harmonic Balance Method

This section presents the results of nonlinear simulations performed on the WEM of Fig. 4.1. First, a nonlinear simulation is compared with the results of the linear analysis. Then, in subsection 4.4.2, simulations with unbalance on both rotors are presented. The model used for the SFD is the short bearing model presented in section 3.1.1. The effect of the oil viscosity and the clearance of the SFD is studied, the influence of the SQC stiffness is investigated, and finally simulations with different maneuver loads are presented. In subsection 4.4.3 the state-of-the-art models presented in section 3.1.2 are used. The inertia of the fluid film is taken into account and the effect of a circumferential feed groove on the response of the system is studied. Finally, in subsection 4.4.4, two different nonlinear models are used along with a SFD for the ball bearing B3 and the results are compared.

In all the simulations presented, the dynamic condensation introduced in Chapter 2 has been applied. Additionally, parallel processing has been integrated which is specifically useful when the detailed SFD models are being used. The results depicted showcase the maximum amplitude in the y-direction in the first stage of the HP compressor (HPC-S1). When only the 1x harmonic and higher are included in the simulation, the response (either the total response or the response of each harmonic separately) in the y-direction is the same as the response in the x-direction. When the 0x harmonic is included, it causes an anisotropic behavior that makes the response in the two directions different. When the effect of the 0x harmonic is small, that is, when the journal is not highly eccentric, the difference between the two directions is very small. However, as the eccentricity grows, so can the difference. It is up to the user to decide whether to plot the x-direction or not. In this work only the y-direction is shown for the sake of clarity and mainly because the effects observed are the same in both directions.

Regarding the unbalance scenarios, an unbalance can be placed in any of the HPC-S1, LPC-S1 and LPT-S1. The case where the unbalance is placed in all of these positions is referred to as dual unbalance excitation. In this case, the reference rotor (LP) produces 1x, 2x, ... etc. harmonics, while the secondary rotor (HP) produces 1.5x, 3x, ... etc. harmonics.

4.4.1 Comparison with Linear Harmonic Analysis

The linear SFD spring used in the Linear Harmonic Analysis (LHA) is replaced by a nonlinear SFD model, and the results are compared for the same cases described in section 4.3. The SFD has a specific geometry and dynamic viscosity that are regarded as reference values and presented in Table 4.2. Different SFD configurations later on will be clearly indicated.

Table 4.2: Reference SFD values

Reference SFD		
Gap	100	μm
Length	20	mm
Radius	110	mm
Dynamic viscosity	2.5	$mPas$

For the case of the static unbalance located on the LP rotor, the linear damping value of 5 Ns/mm underestimates the amplitude of the L3 peak but still provides a good overall approximation of the nonlinear response as seen in Fig. 4.5. The same behavior is evident in the case of a single unbalance located on the HP rotor. The H4 peak is underestimated in the LHA, but the overall approximation of the nonlinear response is adequate, as seen in Fig. 4.6.

Clearly, a constant damping value of 5 Ns/mm provides a good approximation of the nonlinear response. However, this can only be said if the nonlinear result has been calculated and used as a reference. Without it, it is not possible to know if the constant damping used is a good choice or not. In addition, the response can change drastically with certain parameters and thus linear analysis using a constant damping is not appropriate to capture such variations. This will be showcased further in the next sections.

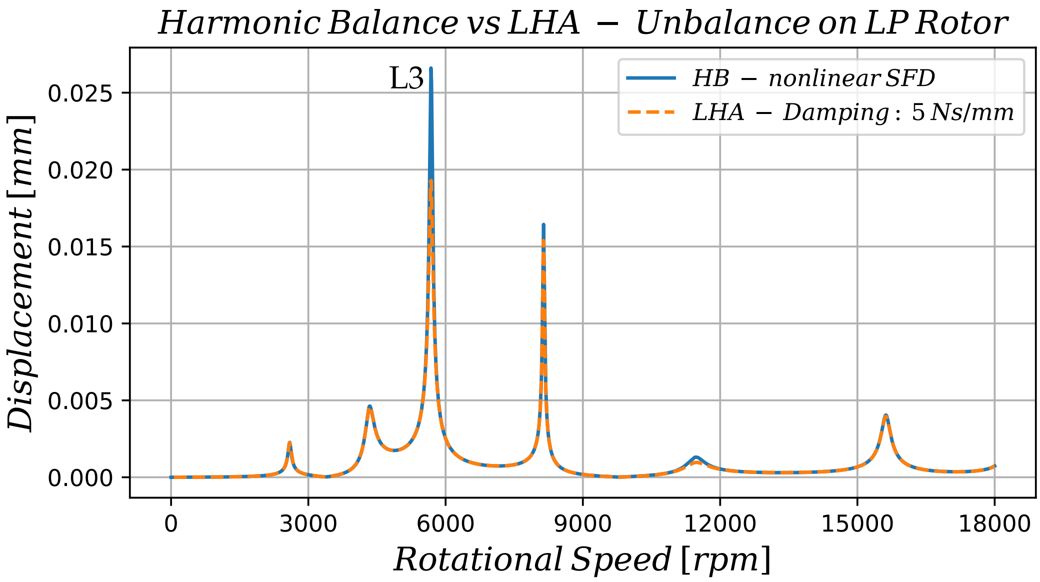

Figure 4.5: Nonlinear vs Linear response of the HPC-S1 for the case of static unbalance located on the LP Rotor.

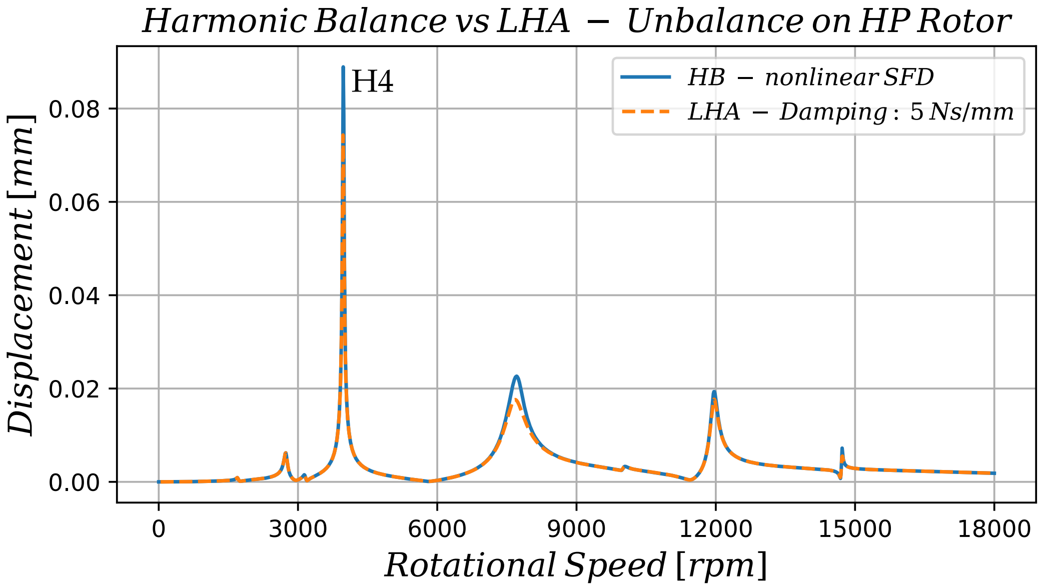

Figure 4.6: Nonlinear vs Linear response of the HPC-S1 for the case of a single unbalance located on the HP Rotor.

4.4.2 Simulations with Dual Unbalance Excitation

Dual unbalance excitation - Reference case

This simulation represents the reference case for the dual unbalance excitation simulations. The SFD parameters follow those in Table 4.2. Three 100 gmm unbalances with zero phase difference are placed at all possible unbalance locations, therefore two unbalance excitations with different frequencies occur.

The result is shown in Fig. 4.7. In addition, the harmonics are plotted separately to clearly show their effect. The 1x harmonic is due to the unbalance excitation from the LP rotor, while the 1.5x harmonic is due to the unbalance excitation from the HP rotor.

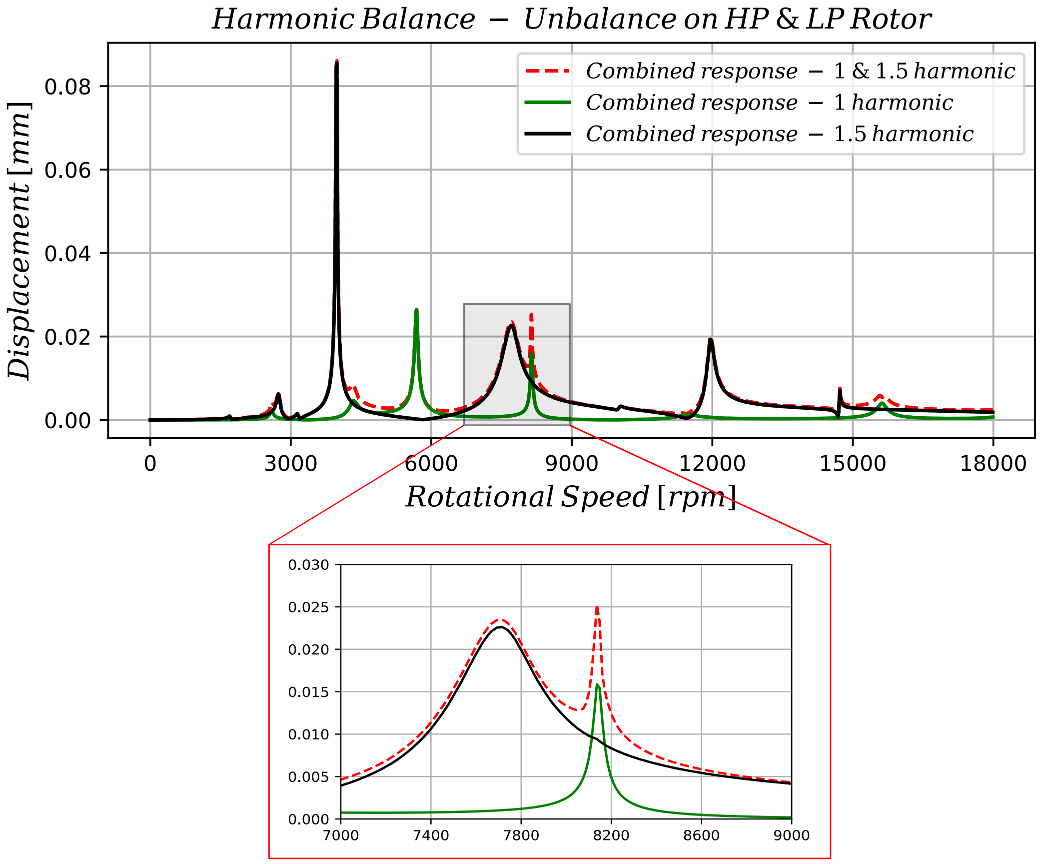

Figure 4.7: Nonlinear frequency response of the HPC-S1 for the reference case of dual unbalance excitation.

All of the observed peaks correspond to the critical speeds shown in the table 4.1. Some resonances seem to be more damped than others and some seem to be expressed as anti-resonances. An interesting observation can be made when looking at the detailed view of the figure above. It can be seen that in the case of dual unbalance excitation, two resonances from separate rotors can be very close to each other and under certain conditions (speed ratio) can coincide, which can lead to unexpected amplitudes and damage to the engine.

Dual unbalance excitation - SFD parameter variation

In the following simulations, the oil viscosity and the radial gap of the SFD are varied. These simulations show how much the response can vary and how difficult it is to replace a nonlinear SFD spring with a linear damping value. In Fig. 4.8 the oil viscosity is varied with the lowest value corresponding to a temperature of about 130 °C and the highest value corresponding to a temperature of approximately 25 °C. The 1x and 1.5x harmonics are shown separately for clarity.

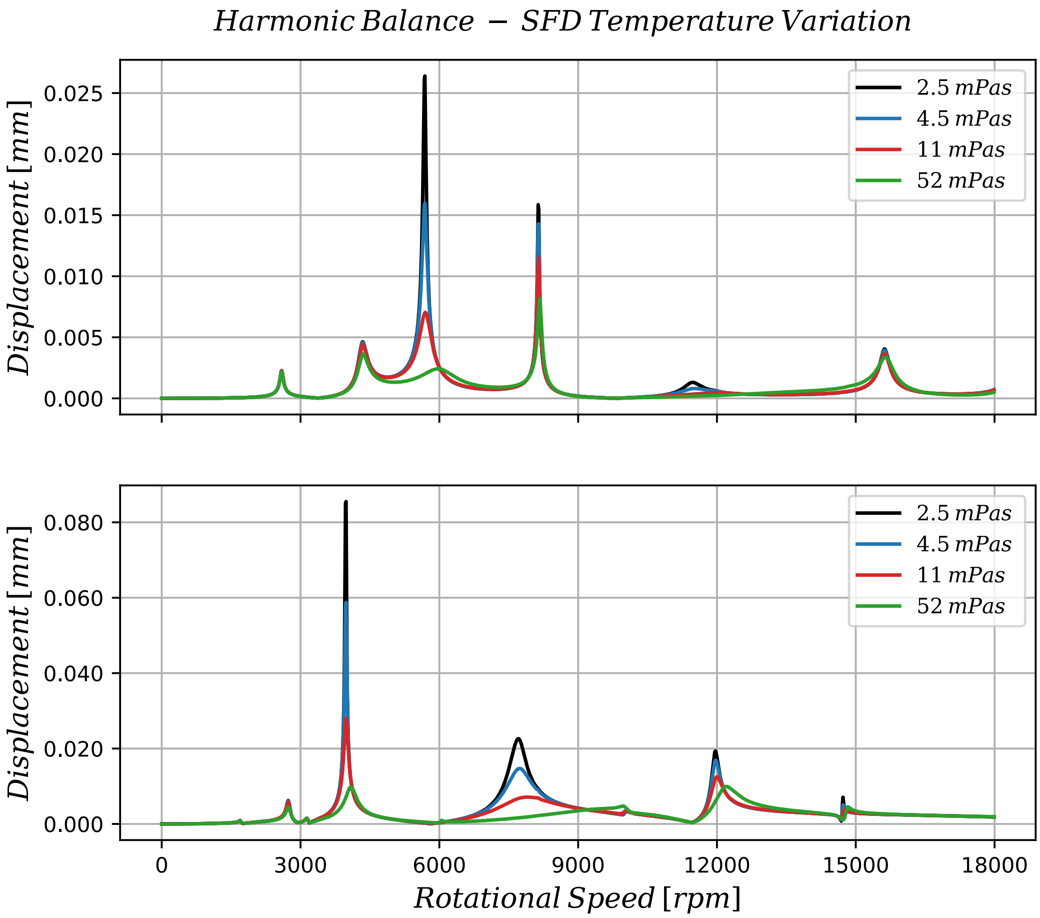

Figure 4.8: Nonlinear frequency response of the 1x (top) and 1.5x (bottom) harmonics for the HPC-S1 in the case of dual unbalance excitation with varying values of SFD oil viscosity.

It is clear that the viscosity of the oil has a strong influence on the response of the system. From a transition from cold to hot oil, the maximum amplitude of the response for both harmonics (L3 and H4 resonances) can experience an increase of approximately 12 and 7.5 times, respectively. In addition, resonances L5 and H6 that were completely damped when the oil was cold, can appear again as the oil warms up. Since the oil can experience all of these states, using a constant damping coefficient value for the SFD does not seem adequate to capture such variations.

A similar influence on the maximum amplitude, but less on the shape of the response, is observed when the gap (clearance) of the SFD is varied from 80 μm to 160 μm. It is reminded that the gap value refers to the radial distance between the journal and the housing when the former is centered within the SFD. As the metal of the journal and housing heats up or cools down during operation, this clearance can vary significantly from its nominal design value. The results are shown in Fig. 4.9.

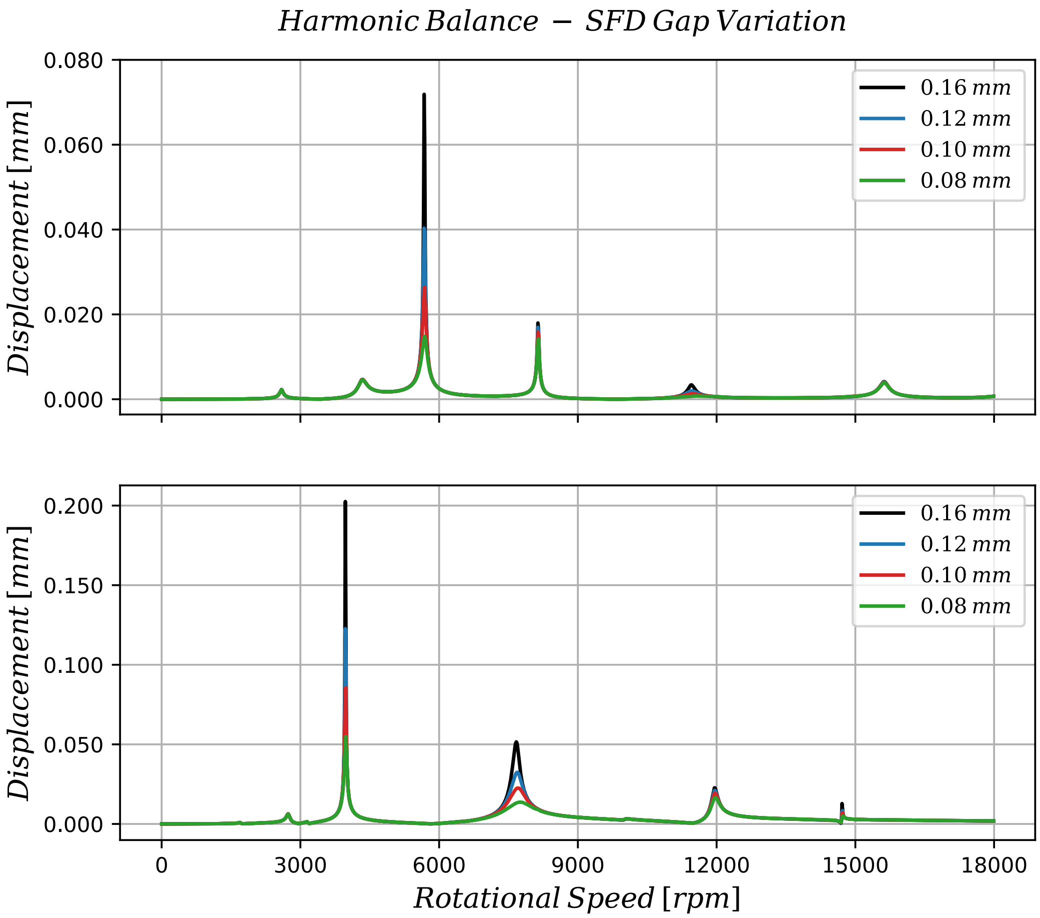

Figure 4.9: Nonlinear frequency response of the 1x (top) and 1.5x (bottom) harmonics for the HPC-S1 in the case of dual unbalance excitation with varying values of the SFD radial gap.

Dual unbalance excitation - SQC stiffness influence

The influence of the SQC support is investigated in the following simulations. Three different cases are considered, one with an SQC stiffness of 25 kN/mm (soft), one with 50 kN/mm (stiff) and one with 75 kN/mm (very stiff). The reference SFD from Table 4.2 is used. The analysis now includes the zero harmonic as well as the 2x and 3x harmonics, for a total of 5 harmonics in this simulation. Fig. 4.10 shows the response of the 1, 1.5 and 0x harmonics for the different cases of SQC stiffness.

Immediately noticeable is that the softer support allows more movement of the journal inside the SFD. As a result, the damping force increases and the response amplitude decreases. A cage that is too stiff can render the SFD ineffective, as shown in Fig. 4.10, where the maximum amplitude of the 1.5 x harmonic exceeds 120 μm. Thus, an important conclusion is that the SQC has a strong influence on the response and damping of the critical modes, and thus its design should be done in conjunction with the design of the SFD.

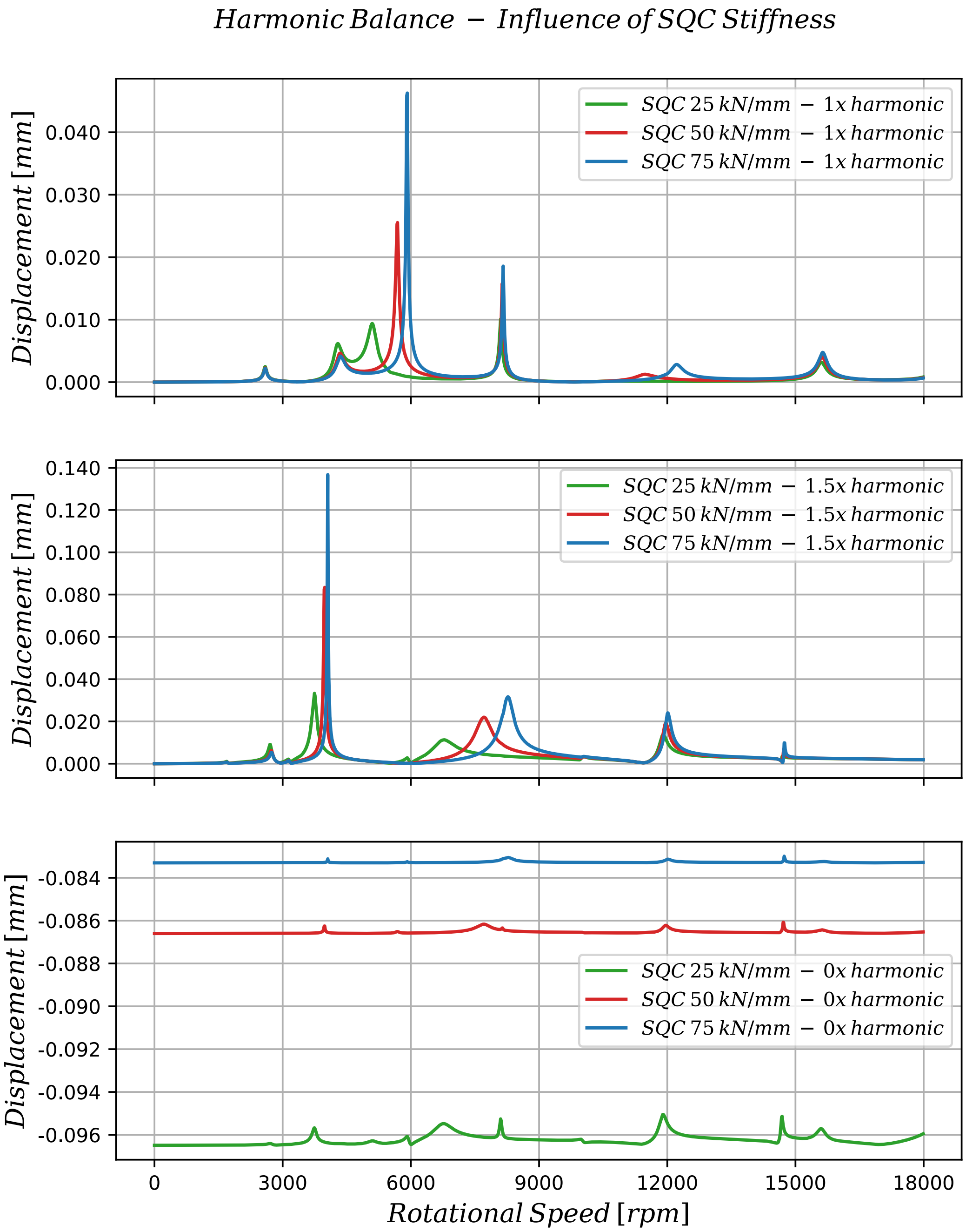

Figure 4.10: Nonlinear frequency response of the 1x, 1.5x and 0x harmonic for the HPC-S1 in the case of dual unbalance excitation with varying values of the SQC stiffness

The 0x harmonic also appears to affect the response of the system, as shown in the lower diagram of Fig. 4.10. For the case of a very stiff SQC, the 0x response is almost a flat line, meaning that it is mainly influenced by the weight of the engine, which remains constant throughout the simulation. As the SQC becomes softer, the 0x response deviates from that of a flat line and shows peaks due to the nonlinear force, which also contributes a 0x component in addition to the weight. The influence of this specific harmonic becomes even greater when high G-loads are applied, as will be showcased later.

Finally, compared to the importance of the 0x, 1x and 1.5x harmonics, the 2x and 3x harmonics shown in Fig. 4.11 have a negligible effect in this particular case and will not be shown further.

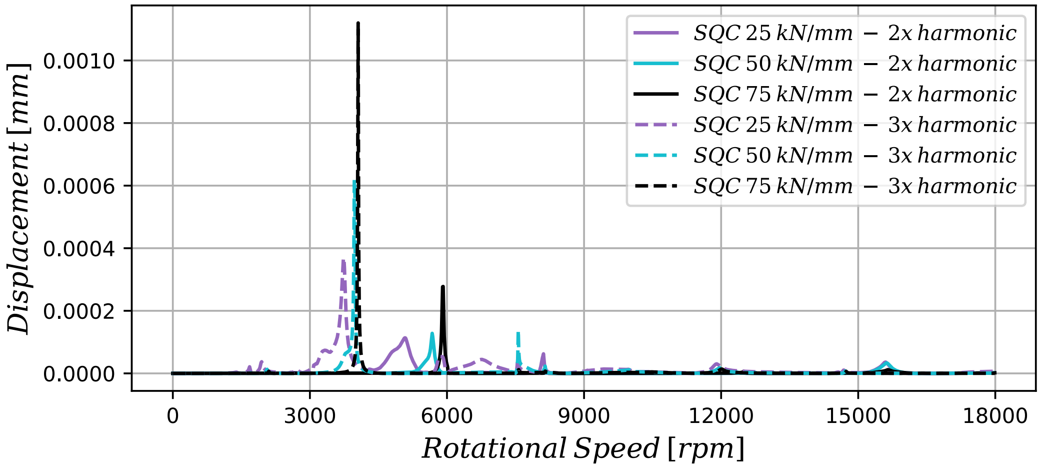

Figure 4.11: Nonlinear frequency response of the 2x and 3x harmonic for the HPC-S1 in the case of dual unbalance excitation with varying values of the SQC stiffness

Dual unbalance excitation - Influence of maneuver loads

An aircraft engine may experience high G-forces during operation, such as when the aircraft is maneuvering. During a maneuver, the increased G-load causes the journal to be pushed toward the SFD housing, increasing its eccentricity. The higher the G-load, the more pronounced this behavior becomes.

In the following cases, the effect of such high G-loads on the response of the system is examined in conjunction with the SQC support stiffness. It should be noted that the response of the 0x harmonic has been normalized to zero speed, i.e. at zero speed the displacement is also zero. This allows for a better understanding of the significance of the 0x harmonic.

In the first case, shown in Fig. 4.12, a stiff SQC (50 kN/mm) is used and a maneuver load of 4G is implemented. The results are compared to the case of a normal 1G load on the engine. It is clear that the 0x harmonic changes significantly when a higher G-force is applied, and this also affects the other harmonics, namely the 1x and the 1.5x, where their maximum amplitudes are reduced by approximately 40 % and 38 %, respectively. Since the SQC is very stiff, the shape of the 1x and 1.5x response curves is not greatly altered. However, the same cannot be said for the response curve of the 0x harmonic. In addition, compared to the 1G case, the magnitude of the 0x harmonic in the 4G case increases to the same order of magnitude as the 1x and 1.5x responses.

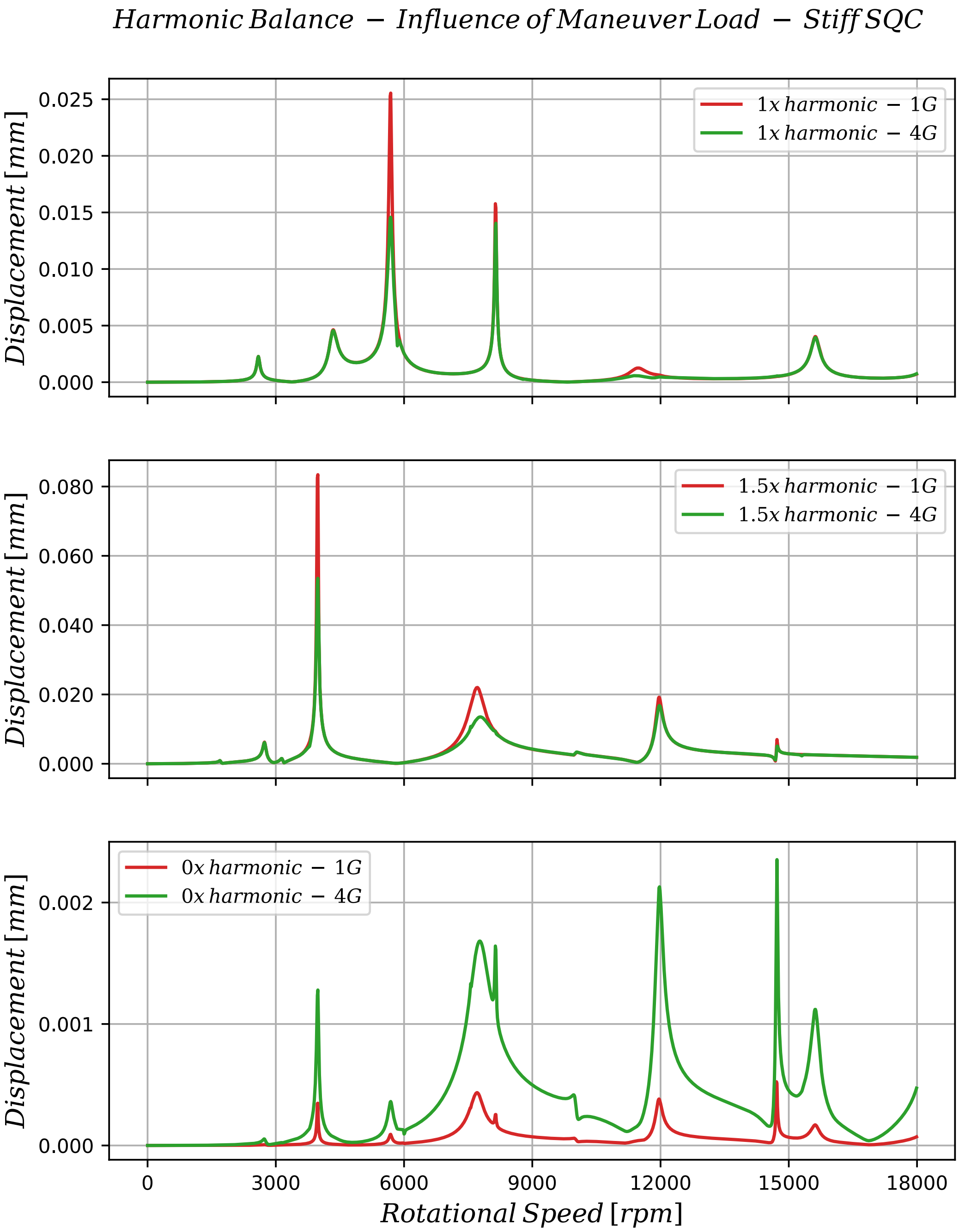

Figure 4.12: Nonlinear frequency response of the 1x, 1.5x and 0x harmonic for the HPC-S1 for a maneuver load of 4G, using a stiff SQC.

In the second case, presented in Fig. 4.13, a soft SQC (25 kN/mm) is used. Since the journal is forced to reach higher eccentricities within the SFD compared to the case of the stiff SQC, the effect of the maneuver load becomes greater. Now, the amplitude of the 0x harmonic is almost half of the amplitude of the 1.5x harmonic and even exceeds the amplitude of the 1x harmonic for most of the frequency range. Furthermore, compared to the previous case, the 0x harmonic affects the response curves of the 1x and 1.5x harmonics not only in amplitude but also in shape.

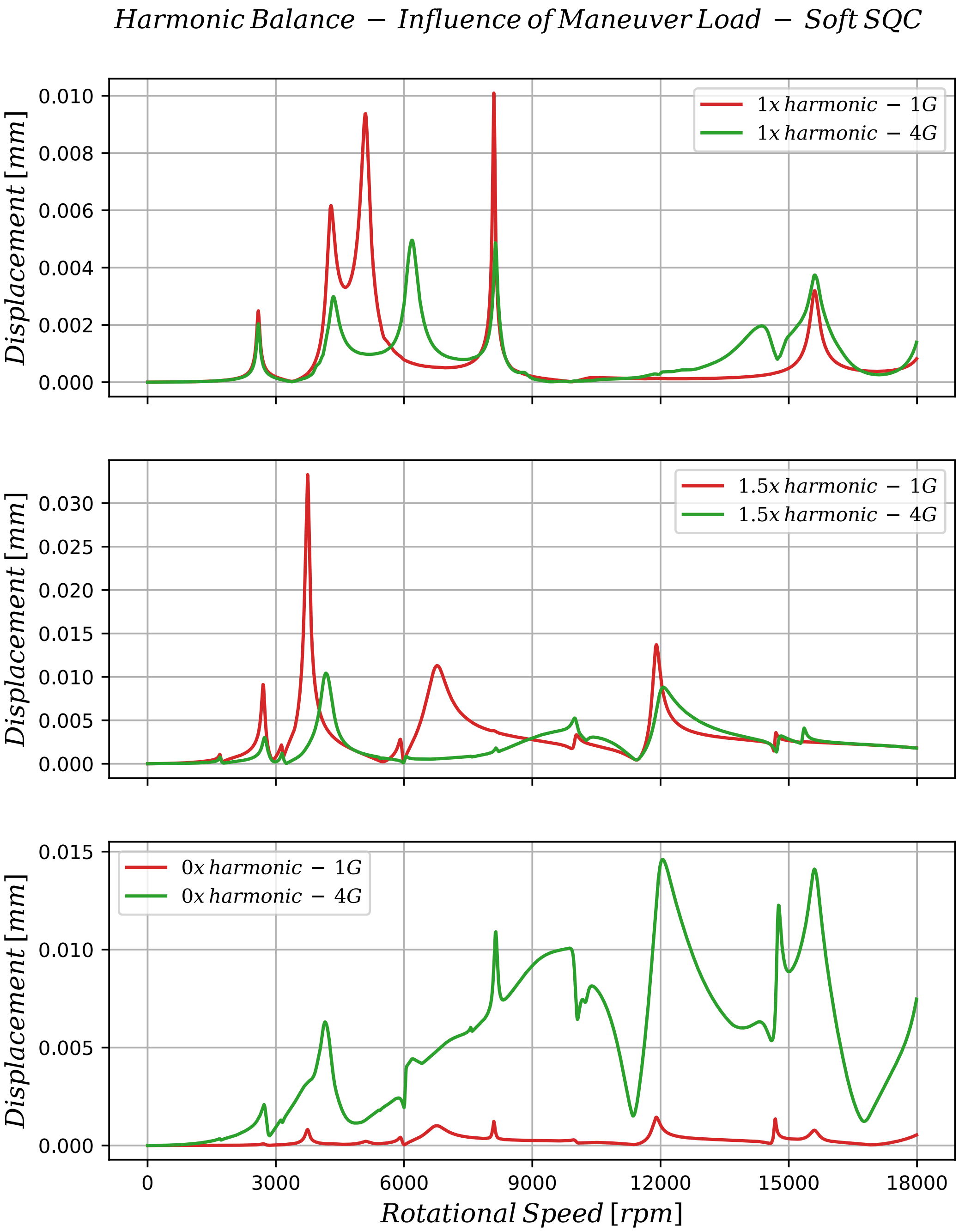

Figure 4.13: Nonlinear frequency response of the 1x, 1.5x and 0x harmonic for the HPC-S1 for a maneuver load of 4G, using a soft SQC.

The effect of lower G loads is also examined for the soft SQC case in Fig. 4.14. Here, only the response of the 1.5x harmonic is shown, since it provides higher vibration amplitudes compared to the 1x. Once again, the influence of the G-load is clear. In the case examined here, even a small 2G load can significantly affect the response amplitudes. All of the simulations performed here demonstrate the importance of including the 0x harmonic in the harmonic balance simulations. A static calculation and its addition to the final response is not sufficient to represent the complex relationship between the 0x and the rest of the harmonics.

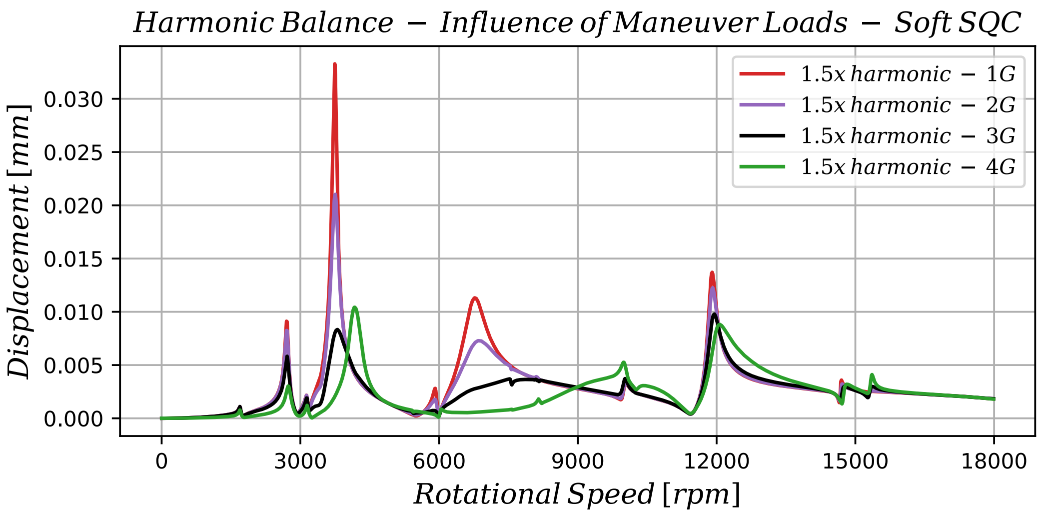

Figure 4.14: Nonlinear frequency response of the 1.5x harmonic for the HPC-S1 for a maneuver load of 1, 2, 3 and 4G, using a soft SQC.

4.4.3 Simulations using State-of-the-Art SFD Models

In this section, the simulations use the state-of-the-art (detailed) models described in 3.1.2 to calculate the SFD reaction forces. Compared to the short-bearing approximation, they provide a high level of detail at the cost of increased simulation effort. First, different modeling approaches for different cavitation boundary conditions (BCs) are compared. Then, a circumferential groove is added and inertia effects are considered. Finally, the effect of the groove depth is investigated.

The oil temperature is kept constant at 120 ^oC in the first simulations to approximate the viscosity of Table 4.2 and is later reduced to 40 ^oC to better show specific effects. Therefore thermal modeling is not presented in this work. This is due to the significant simulation effort required. An unbalance of 100 gmm is placed on the HPC-S1 and only the 1x harmonic is considered in order to reduce simulation time. In all the simulations presented, a stiff SQC of 50 kN/mm is used. A feed hole is considered for the lubricant supply and the relative pressure outside the SFD is 0 Pa.

Detailed SFD models - Influence of modeling approach and cavitation boundary conditions

The modeling approach can either be the short bearing approximation or the finite bearing solution. For both approaches, the solution is numerical, but in the short approximation, the Reynolds equation has been simplified before. For the cavitation boundary condition (BC) in the latter approach, the Gümbel and the Reynolds conditions are compared. The results are presented in Fig. 4.15.

The difference between the three models is marginal. The modeling improvement from short to finite bearing as well as from Gümbel to Reynolds cavitation condition does not seem to affect the response of the system. This observation may be true for this specific case, but should not be generalized in any way.

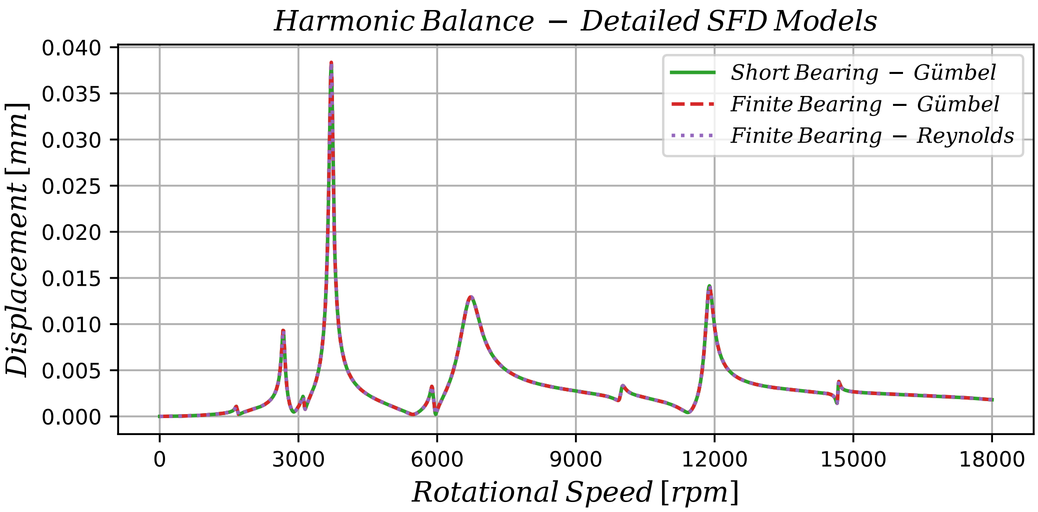

Figure 4.15: Nonlinear frequency response of the HPC-S1 using detailed SFD models with different cavitation conditions.

Detailed SFD models - Influence of groove and inertia effects

Now a circumferential groove is added to the SFD with a length and depth of 10 mm. Initially, no inertia model is used. Then the temporal inertia is considered and finally a simulation around the H4 resonance is performed including the convective inertia. This last case is called full inertia and due to the increased simulation time, it would not be efficient to simulate the whole speed range. The cavitation model used is Gümbel. The results are shown in Fig. 4.16.

The black line represents an SFD without groove and inertia modeling. The entire length of the SFD is used to generate pressure, so the reaction forces are high. Coupled with the low temperature of the oil, which is reflected in a high viscosity, the vibration amplitude is kept to a minimum. Considering a groove with a length of 10 mm, the effective length of the SFD is significantly reduced. If the inertia is not modeled, this results in lower reaction forces and therefore a very different response with much larger amplitudes (green line). When the inertia is considered, the additional mass created by the groove contributes to the pressure generation and the reaction forces are higher compared to the case where no inertia is modeled. The response where only the temporal inertia is simulated corresponds to the red line. However, this inertia model [6] should be limited to small vibration amplitudes. A better approach is to use the full inertia model [29], which also includes the convective inertia term and corresponds to the blue line. The difference with the previous model is significant, as shown in the detailed view of Fig. 4.16.

The simulations presented in Fig. 4.16 demonstrate the importance of inertia modeling. If the simulation time for the full range is not acceptable, the author suggests local runs around the resonance peaks of interest where the inertia is modeled. The difference between temporal and full inertia seems to be significant in the response of the system, but a general conclusion is not yet possible. A general approach is to use the temporal inertia first, which provides a faster simulation compared to the full model, and then use the full model only at high amplitude resonance peaks.

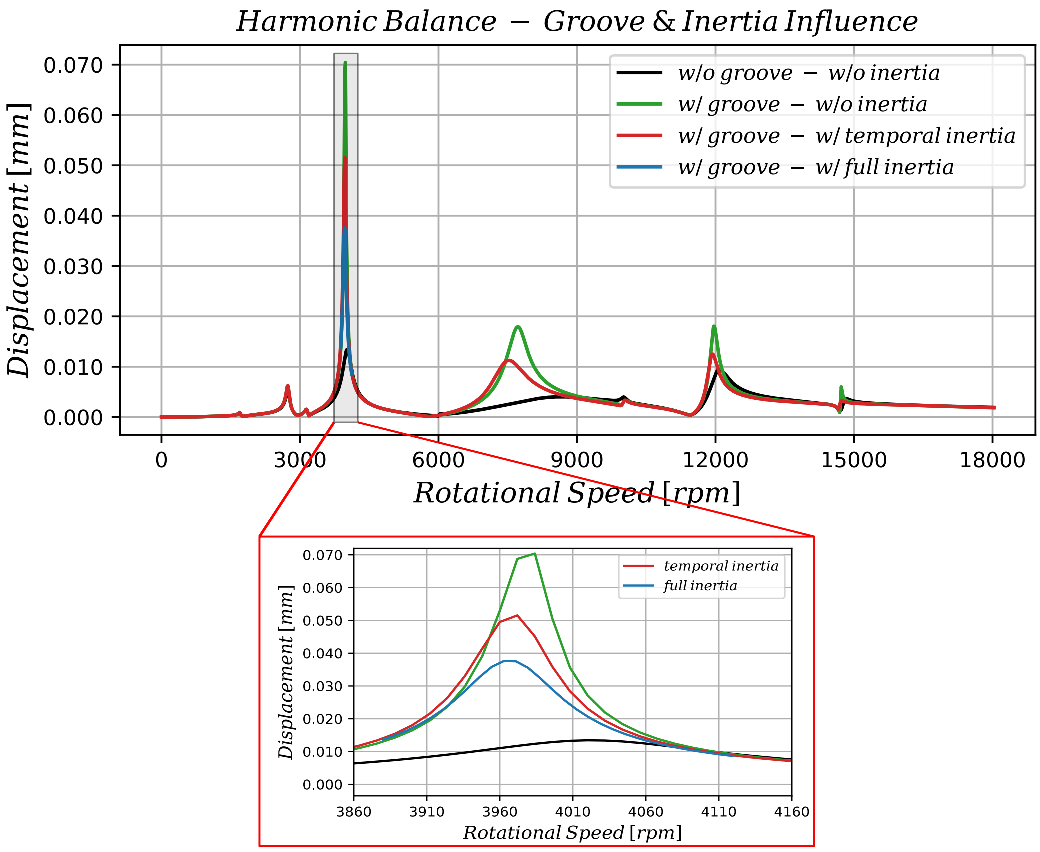

Figure 4.16: Nonlinear frequency response of the HPC-S1 using a detailed SFD model with a circumferential groove of 10mm in length and inertia effects.

Detailed SFD models - Influence of groove depth

The influence of the circumferential groove depth is investigated. Tan and Li state that the groove depth doesn't appear to have a significant effect on the unbalance response of the system [58]. The results shown in Fig 4.17 agree with this claim.

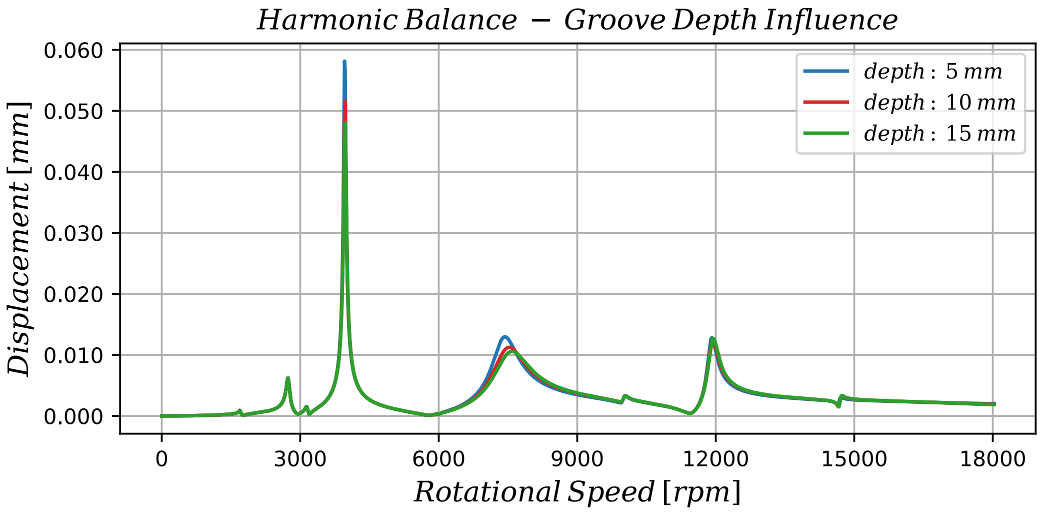

Figure 4.17: Nonlinear frequency response of the HPC-S1 using a detailed SFD model with a circumferential groove of various depth values.

There is a reduction in the H4 and H5 resonance amplitudes when the depth is increased from 5 mm to 10 mm, but a further increase to 15 mm only improves the damping quality of the SFD by a small amount. This behavior can be explained by the concept of effective groove depth [2]. A recirculation region is formed inside the groove which limits further dynamic pressure generation after a specific depth. In the case examined here, it seems that the effective groove depth is around 15 mm, although further investigation is required to reach a conclusion, since the different temperatures occurring in the oil film may also influence this parameter.

4.4.4 Simulations using Nonlinear Ball Bearing Models

The rolling element bearing models discussed in Chapter 3 are integrated into the harmonic balance simulations by replacing the B3 spring, shown in Fig. 4.1. The geometry of the bearing corresponds to a typical bearing used in aircraft engine applications and the preload in the axial direction given for both models is 136 μm. The reference SFD is used with the short bearing model for the calculation of its reaction forces. The stiffness of the SQC is 25 kN/mm. An unbalance of 100 gmm is placed on the HPC-S1 and the 1x harmonic is included in the analysis. Three additional simulations were performed with constant B3 typical stiffness values to investigate the influence of using the nonlinear REB models in this particular case. The results are presented in Fig. 4.18, while the detail views A and B are shown in Fig. 4.19.

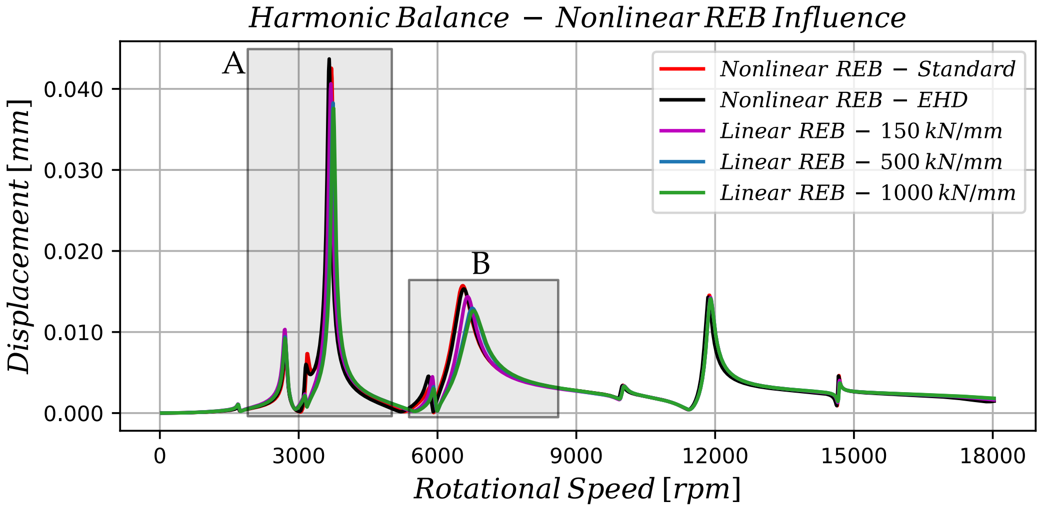

Figure 4.18: Nonlinear frequency response of the HPC-S1 using a detailed SFD model with a circumferential groove of various depth values.

In the case presented, there seems to be no significant difference between the two nonlinear REB models. In detailed view A, the amplitude of the compressor when using the EHD model is slightly higher than the amplitude calculated with the standard model. This is also observed in some other peaks, but the opposite is also true, as can be seen in the peak of the detailed view B, where the EHD produces a smaller vibration amplitude compared to the standard model. The latter is expected since the EHD produces damping due to the lubricant. The former behavior is counterintuitive, but if the damping force provided by the EHD model is neglected, the behavior persists. Therefore, it can

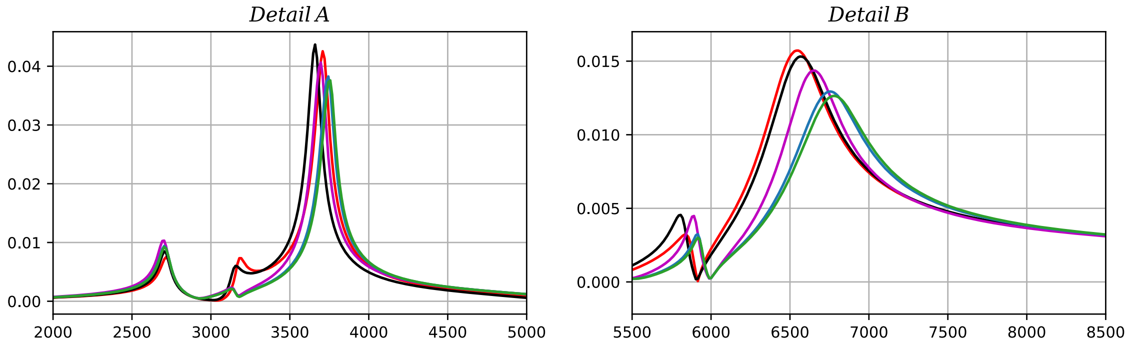

Figure 4.19: Detailed views A (left) and B (right) of nonlinear response using rolling element bearings.

be concluded that the bearing is stiffer at this specific resonance, but the phenomenon requires further investigation beyond the scope of the present thesis.

Comparing the responses using a constant stiffness value for the REB with the results using the nonlinear models shows that there is a difference that may be neglected in the very early design stages, but is important for the detailed design. It is easy to observe that by running one or two simulations using the ball bearing model, a constant stiffness value can be fine-tuned to adequately approximate the true response. This value can then replace the ball bearing at the beginning of the design when multiple simulations are required.

It is also important to note that even with the presence of a squirrel cage, whose stiffness largely determines the stiffness of the entire SFD configuration, the stiffness of the ball bearing still has an effect on the final response. If all the other bearings in the engine were modeled, this effect could be much greater. However, more research is needed to support this claim.

Finally, an interesting observation is that higher stiffness does not necessarily mean higher amplitudes. Although this is true for 1-degree-of-freedom systems, for large multi-degree-of-freedom systems, modal stiffness plays a more significant role in determining amplitude than physical stiffness alone.

5 The Harmonic Balance Method in Surrogate Modeling Approaches

The purpose of this chapter is to briefly introduce the potential of the harmonic balance method using dynamic condensation in the training of surrogate models based on neural networks. A surrogate model is a model that is used in place of a physical model to predict certain outputs from certain inputs. This model acts as a black box. The results presented in this chapter were obtained in collaboration with F. Tieleman, who focused on machine learning methods for aircraft engine rotor optimization [59].

5.1 SFD Surrogate Model

The first surrogate model created was the simplest and was able to predict the SFD reaction forces with an accuracy of about 65 %. The model was trained on a specific SFD geometry following the reference values in Table 4.2 with the only difference that the radius was 80 mm instead of 110 mm.

The model could accept three inputs. These were the relative eccentricities of the journal in the x and y directions and the whirling frequency. The training data was obtained by sampling 10000 input sets using the Latin Hypercube approach [42]. The reaction forces were calculated using the detailed SFD calculation tool with the Gümbel cavitation condition. In this tool, the short bearing approach was chosen, i.e. the Reynolds equation was simplified accordingly but was solved numerically.

To test the potential of the surrogate model, the rotor dynamic model of the HP rotor shown in the work of [45] was used. The two SFDs were replaced by the surrogate model and the case of static unbalance with 500 gmm per unbalance node was examined. The results were compared with the reference case simulated by the harmonic balance method with appropriate dynamic condensation. The SFD model used for the reference simulation was the short bearing model. The result of the comparison is shown in Fig. 5.1.

With the use of the surrogate model, the large resonance peak and the jump phenomenon occurring around 13000 rpm are significantly well captured. However, the prediction of the lower amplitude resonance just after 20000 rpm is not as good as the reference case. Considering the low accuracy of the surrogate, the overall response is adequately predicted and the potential of such models is highlighted. It should also be noted that the simulation using the surrogate model was about 50 % faster than the simulation using the short-bearing approximation, which is already fast due to the analytical formulas.

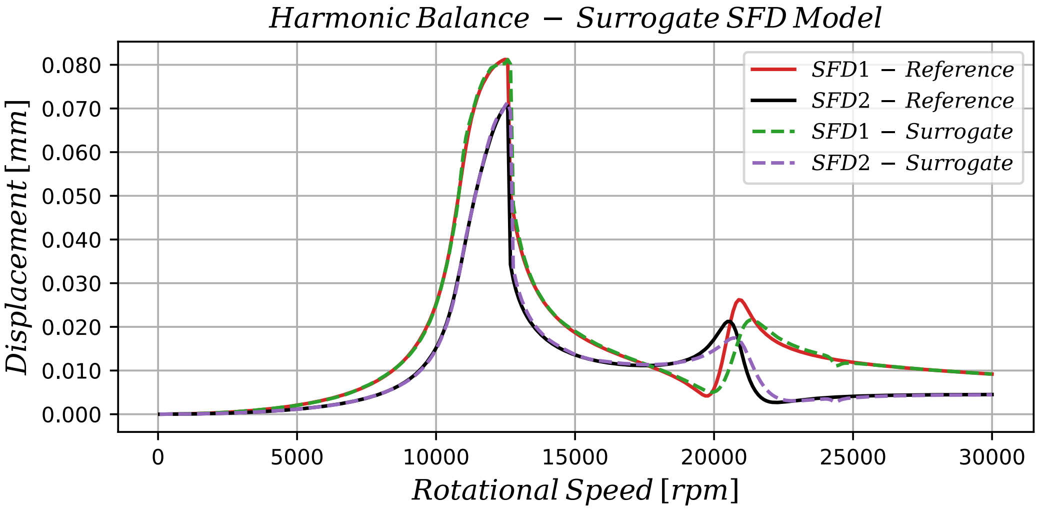

Figure 5.1: Nonlinear frequency response on the 2x SFD nodes when using the short bearing model (solid lines) and the surrogate model (dashed lines) to calculate the SFD reaction forces.

5.2 Peak-Prediction Surrogate Model

The second surrogate model created was intended to replace the entire dynamic simulation of the generic whole engine model shown in Fig. 4.1. The inputs were the geometry of the SFD, specifically the length L, the gap c_r and the radius R. The temperature was kept constant at 60 ^oC. The outputs were the 2 maximum peaks in the HPC-S1 and the 2 maximum peaks in the HPT-S1, a total of 4 outputs.

The model was trained using the results of 800 simulations of the generic dual-spool model. The simulations were again performed using the improved harmonic balancing method presented in this thesis. The short bearing model was used for the SFD force calculations and only the 1x harmonic was included in the analysis. To obtain the desired outputs, the response at the HPC-S1 and HPT-S1 was calculated and the 2 maximum amplitudes from each response were selected. The resulting surrogate model showed a significant accuracy of approximately 90 %.

Leveraging the quality of the surrogate, a sensitivity analysis was performed in order to evaluate the effect of the SFD geometry parameters in attenuating the 4 desired maximum amplitudes in the compressor and turbine stages. A result of this analysis was the first-order Sobol's indices, which show the variance of an output due to the variance of the inputs. An easier way to understand this result is through the heatmap of Fig. 5.2.

The first row (S_1) shows the first order relationship between the inputs and the outputs. The second row (S_T) shows the higher order relations. If $S_1 = S_T$, the relationship is purely linear. If S_1 is close to zero and S_T is not, it means that there are mainly higher order interactions. If both S_1, S_T are close to zero, it means that the output does not vary when the respective input is varied. An interesting observation can be made for the 2nd maximum peak c_2 of the HPC-S1. Its amplitude seems to have mainly a nonlinear relationship with the gap or the length. On the contrary, it changes insignificantly when the radius is varied. For a visual representation, 5 different cases of constant length were

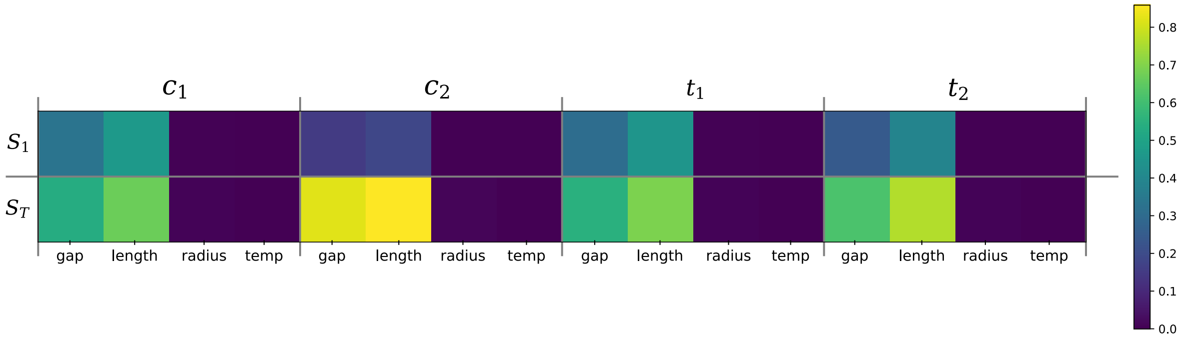

Figure 5.2: Heatmap of first-order (top row) and total-order (bottom row) Sobol's sensitivity indices showing the order of the interaction between each output and the individual inputs (temperature is always constant).

selected and the gap was allowed to vary. Similarly, another 5 cases of constant gap were selected and the length was allowed to vary. In all cases the radius was kept constant. The effect on the amplitude of the c_2 peak is shown in Fig. 5.3.

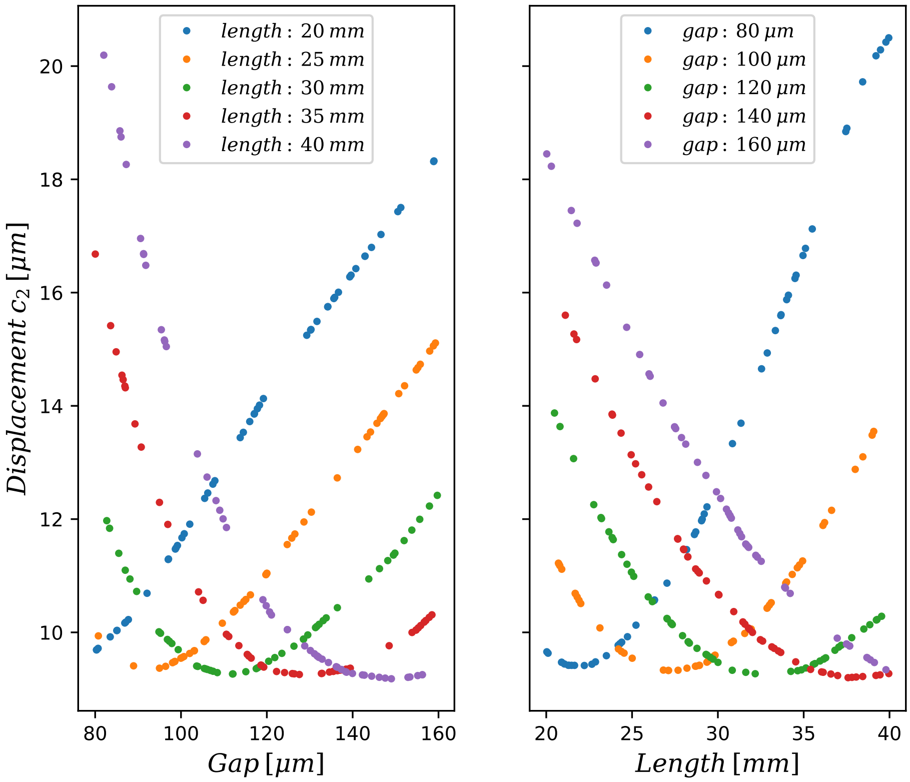

Figure 5.3: Variation of the c_2 amplitude with respect to SFD gap (left) and SFD length (right) for 5 cases of constant SFD length and SFD gap respectively.

The nonlinear relation between the inputs and the output is clear. However, there is also a linear component present which is visible in some cases, for example in the case of $L = 20mm$ in the left figure. Another interesting observation is that for most of the cases presented, there is an optimum value for which the response is minimal. In other words, increasing the length or decreasing the gap as much as possible to increase the damping of the SFD is not always beneficial and can lead to the opposite results.

5.3 Curve-Prediction Surrogate Model

The third surrogate model created is very similar to the second, except that the outputs now are not the maximum amplitude values, but rather the entire frequency response curve of the HPC-S1 and HPT-S1. The inputs remain the same and the model is now trained on 200 simulations of the generic dual-spool engine model. The resulting surrogate shows a very high accuracy of 97 %. This means that the predicted curves are almost identical to those calculated by the physical model, as shown in Fig. 5.4.

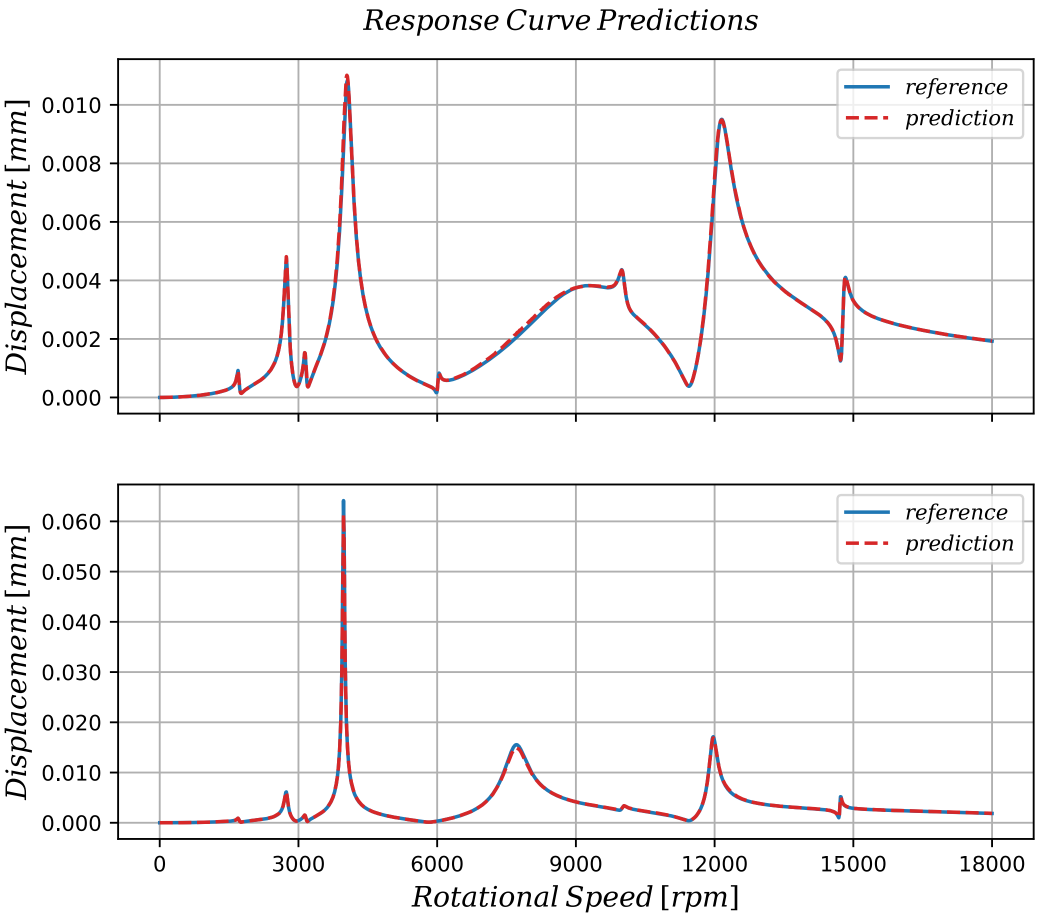

Figure 5.4: Predictions of the HPC-S1 nonlinear frequency response using the surrogate model and comparison with the results from the physical calculation.

6 Conclusions and Outlook

6.1 Conclusions

This thesis investigated the nonlinear steady-state response of a generic whole engine model using the harmonic balance method with appropriate condensation.

Using both the short and the detailed SFD models, various simulations were performed under different unbalance scenarios and SFD geometric and operating parameters. The effects of oil viscosity, radial clearance size, feed groove and oil inertia were studied, along with the effect of the SFD support stiffness on the system response, especially under high G-load conditions that occur during aircraft maneuvers. The effect of modeling the ball bearing was also investigated using two different approaches. Approximately half of the results presented were performed under multiple frequency excitation resulting from unbalance on both rotors. According to the simulation results of the generic engine model presented in Chapter 4, the author arrives at five main conclusions:

- The effect of the 0x harmonic is very significant and cannot be replaced by a static calculation. Simulations under increasing G-loads show that there is a significant influence of the 1x and 1.5x components, which becomes larger the softer the squirrel cage is. A static calculation cannot capture this complex relationship.
- The stiffness of the squirrel cage support greatly influences the response of the system and should be designed in conjunction with the SFD. Simulations showed that an excessive amount of stiffness can render the SFD ineffective and significantly increase the amplitudes of the 1x and higher components. On the other hand, a softer support allows for more movement of the journal within the SFD, resulting in higher damping forces and lower vibration amplitudes.
- A more detailed modeling of the SFD cavitation condition won’t necessarily affect the dynamic response to a large extent.
- Modeling of the fluid inertia must be considered, especially if there is a feed groove in the SFD. Otherwise, the groove will reduce the effective length of the SFD, resulting in lower damping forces than in reality and incorrect response prediction. Regarding the inertia model, Between the temporal and full inertia modeling, there is a significant difference between the time and full inertia models when comparing the vibration amplitude of the largest resonance.
- Nonlinear ball bearing models should be included in the simulations as their influence can become important even with a moderately stiff SQC. For the particular engine model, the modeling approach for the bearing showed very small differences between them. The nonlinear result can be used to fine-tune a constant

stiffness value that can be used in the early design stages to reduce simulation time.

Finally, the work presented in Chapter 5 aims to highlight the use of the method in training surrogate models. Due to its computational efficiency, predictive models can be trained in a matter of hours. As the results show, even models of low accuracy can still be effectively integrated into the nonlinear simulations and produce results at a fraction of the cost. However, further investigation on the matter is required. The author concludes that surrogate models could be very useful for efficiently integrating THD SFD models into the harmonic balance calculations, since they are computationally expensive due to their complexity and a time-transient solution wouldn't be viable for the design stages.

6.2 Outlook: The Next Steps

The author recognizes the potential of the method and suggests the next steps following this thesis.

First, the contacts between the journal and the housing within the SFD need to be modeled. This is a necessary addition in order to simulate engine response with unsupported SFDs, i.e. SFDs where the journal is not supported by a squirrel cage. Currently, such configurations can be simulated using a very soft squirrel cage, but this is not the ideal approach and does not apply to every SFD geometry. Since the journal is allowed to reach very high eccentricities, this causes the solution to diverge at certain frequencies due to the fact that the journal is very close to the housing and in reality there is contact.

The second addition is the modification of the method to allow for quasi-periodic solutions. As described in Chapter 2, these solutions can occur when the speed ratio of the shafts cannot be expressed as a ratio of integers. Under this condition, there is no number of sampling periods that can be chosen to avoid truncation of the secondary signal, so the resulting signal will be quasi-periodic. Fortunately, there is a way to account for quasi-periodic solutions using an extension of the harmonic balance method. The idea is based on the concept of multidimensional time, where essentially each signal is observed on its own time domain, then a 2D Fourier transform is performed, and the resulting solution is now a surface containing the Fourier coefficients for linear combinations of the harmonics of each signal. A very good amount of literature exists on the subject [34, 52, 24, 37]. In addition to the quasi-periodic solution extension, an evaluation of the stability of the equilibrium positions computed by the harmonic balance method must be implemented using Floquet theory.

It is also recommended to implement an adaptive step solver using a continuation scheme. This can lead to increased efficiency since the frequency step can be increased in the part of the simulation where the response is flat and no sharp resonances occur. In addition, a continuation scheme can capture unstable solutions.

Finally, a large improvement in efficiency can be achieved by implementing Model Order Reduction (MOR) schemes (Guayn, Craig-Bampton). Such reduction schemes can be applied to the linear part of the system that is left after partitioning the degrees of freedom. For the model presented in this thesis, a reduction in the linear part may sound insignificant, since the linear system solved to compute the Fourier coefficients for the linear degrees of freedom is already very fast. However, in more detailed real jet engine models, the casings typically have thousands of degrees of freedom due to their modeling complexity. This is where MOR methods can provide high computational savings.

References

[1] Lysandros Anastasopoulos and Athanasios Chasalevris. Bifurcations of Limit Cycles in Rotating Shafts Mounted on Partial Arc and Lemon Bore Journal Bearings in Elastic Pedestals. *Journal of Computational and Nonlinear Dynamics*, 17(6):061003, 03 2022.

[2] Luis San Andres. Force coefficients for a large clearance open ends squeeze film damper with a central feed groove: Experiments and predictions. *Tribology International*, 71:17–25, 2014.

[3] Luis San Andrés, Sung-Hwa Jeung, Sean Den, and Gregory Savela. Squeeze film dampers: An experimental appraisal of their dynamic performance. 2016.

[4] L. San Andrés. Notes 13: Squeeze film dampers, 2010.

[5] L. San Andrés. Notes 2: Classical lubrication theory, 2010.

[6] Luis San Andrés and Adolfo Delgado. A Novel Bulk-Flow Model for Improved Predictions of Force Coefficients in Grooved Oil Seals Operating Eccentrically. *Journal of Engineering for Gas Turbines and Power*, 134(5):052509, 03 2012.

[7] MVS Babu, A Rama Krishna, and KNS Suman. Review of journal bearing materials and current trends. *American Journal of Materials Science and Technology*, 4(2):72–83, 2015.

[8] Philip Bonello and Pham Minh Hai. Computational Studies of the Unbalance Response of a Whole Aero-Engine Model With Squeeze-Film Bearings. *Journal of Engineering for Gas Turbines and Power*, 132(3):032504, 12 2009.

[9] Philip Bonello and Pham Minh Hai. A receptance harmonic balance technique for the computation of the vibration of a whole aero-engine model with nonlinear bearings. *Journal of Sound and Vibration*, 324(1):221–242, 2009.

[10] Lukas Braun. Aircraft engine rotor modelling and analyses with flexibility matrices. Master's thesis, Universität Stuttgart, 2021.

[11] T. M. Cameron and J. H. Griffin. An Alternating Frequency/Time Domain Method for Calculating the Steady-State Response of Nonlinear Dynamic Systems. *Journal of Applied Mechanics*, 56(1):149–154, 03 1989.

[12] Athanasios Chasalevris and Fadi Dohnal. Improving stability and operation of turbine rotors using adjustable journal bearings. *Tribology International*, 104:369–382, 2016.

[13] R. Davis, R.D. Henshell, and G.B. Warburton. A timoshenko beam element. *Journal of Sound and Vibration*, 22(4):475–487, 1972.

[14] A Dinc. The effect of flight and design parameters of a turbofan engine on global warming potential. *IOP Conference Series: Materials Science and Engineering*, 1051(1):012051, feb 2021.

[15] D. Dowson. A generalized reynolds equation for fluid-film lubrication. *International Journal of Mechanical Sciences*, 4(2):159–170, 1962.

[16] D.J. Ewins. Control of vibration and resonance in aero engines and rotating machinery – an overview. *International Journal of Pressure Vessels and Piping*, 87(9):504–510, 2010. Dynamic Loading of Components and Structures.

[17] Chengye Fan, Ruoshui Jiang, and Songzhi Zhang. Current status and future prospects of jet engines. *Highlights in Science, Engineering and Technology*, 29:240–246, Jan. 2023.

[18] Tieshu Fan, Sina Hamzehlouia, and Kamran Behdinan. The effect of lubricant inertia on fluid cavitation for high-speed squeeze film dampers. *Journal of Vibroengineering*, 19, 12 2017.

[19] Michael I. Friswell, John E. T. Penny, Seamus D. Garvey, and Arthur W. Lees. *Dynamics of Rotating Machines*. Cambridge Aerospace Series. Cambridge University Press, 2010.

[20] Stanislav Fábry and Marek Češkovič. Aircraft gas turbine engine vibration diagnostics. *Magazine of Aviation Development*, 5, October 2017.

[21] Ioannis Gavalas and Athanasios Chasalevris. Nonlinear Dynamics of Turbine Generator Shaft Trains: Evaluation of Bifurcation Sets Applying Numerical Continuation. *Journal of Engineering for Gas Turbines and Power*, 145(1):011003, 10 2022.

[22] Edoardo Gheller, Steven Chatterton, Andrea Vania, and Paolo Pennacchi. Squeeze film damper modeling: A comprehensive approach. *Machines*, 10(9), 2022.

[23] Edoardo Gheller, Steven Chatterton, Andrea Vania, and Paolo Pennacchi. Application of squeeze film dampers. In Athanasios Chasalevris and Carsten Proppe, editors, *Advances in Active Bearings in Rotating Machinery*, pages 111–133, Cham, 2023. Springer International Publishing.

[24] Mikhail Guskov and Fabrice Thouverez. Harmonic Balance-Based Approach for Quasi-Periodic Motions and Stability Analysis. *Journal of Vibration and Acoustics*, 134(3):031003, 04 2012.

[25] E. J. Hahn and P. Y. P. Chen. Harmonic Balance Analysis of General Squeeze Film Damped Multidegree-of-Freedom Rotor Bearing Systems. *Journal of Tribology*, 116(3):499–507, 07 1994.

[26] Pham Minh Hai and Philip Bonello. A Computational Parametric Analysis of the Vibration of a Three-Spool Aero-Engine Under Multifrequency Unbalance Excitation. *Journal of Engineering for Gas Turbines and Power*, 133(7):072504, 03 2011.

[27] S. Hamzehlouia. *Squeeze Film Dampers in High-Speed Turbomachinery: Fluid Inertia Effects, Rotordynamics, and Thermohydrodynamics*. PhD thesis, Mechanical and Industrial Engineering, University of Toronto, 2017.

[28] Sina Hamzehlouia and Kamran Behdinan. Thermohydrodynamic modeling of squeeze film dampers in high-speed turbomachinery. *SAE International Journal of Fuels and Lubricants*, 11(2):129–146, 2018.

[29] Sina Hamzehlouia and Kamran Behdinan. Squeeze film dampers supporting high-speed rotors: Fluid inertia effects. *Proceedings of the Institution of Mechanical Engineers, Part J: Journal of Engineering Tribology*, 234:135065011985579, 06 2019.

[30] Feng He, Paul Allaire, and Timothy Dimond. Use of the harmonic balance method for flexible aircraft engine rotors with nonlinear squeeze film dampers. 8, 08 2014.

[31] A. Homaifar, H.Y. Lai, and E. McCormick. System optimization of turbofan engines using genetic algorithms. *Applied Mathematical Modelling*, 18(2):72–83, 1994.

[32] Yukio Hori. *Hydrodynamic Lubrication*. Springer Tokyo, 1 edition.

[33] D. Jaitner, R. Schönen, G. Knoll, and Adrian Rienäcker. Effiziente finite-elemente-lösung der energiegleichung zur thermischen berechnung tribologischer kontakte. *Forschung im Ingenieurwesen*, 82, 12 2018.

[34] Laura Junge, Christian Frey, Graham Ashcroft, and Edmund Kügeler. A New Harmonic Balance Approach Using Multidimensional Time. *Journal of Engineering for Gas Turbines and Power*, 143(8):081007, 03 2021.

[35] Shaik Karimulla, B.K. Dutta, and G.Gouthaman. Experimental and analytical investigation of short squeeze-film damper (sfd) under circular-centered orbit (cco) motion. *Journal of Vibration Engineering and Technologies*, 8:215–224.

[36] M. Khonsari, E. Booser, and Francis Kennedy. Applied tribology: Bearing design and lubrication, second edition. *Journal of Tribology-transactions of The Asme - J TRIBOL-TRANS ASME*, 124, 04 2002.

[37] Y.B. Kim and S.-K. Choi. A multiple harmonic balance method for the internal resonant vibration of a non-linear jeffcott rotor. *Journal of Sound and Vibration*, 208(5):745–761, 1997.

[38] Neeraj Kumar and RK Satapathy. Bearings in aerospace, application, distress, and life: A review. *Journal of Failure Analysis and Prevention*, 23:915–947, 2023.

[39] Andrew Yee-Tak Leung. An accurate method of dynamic condensation in structural analysis. *Inernational Journal for Numerical Methods in Engineering*, 12:1705–1715, 1978.

[40] Ka Liew, Egel Urip, Song-Lin Yang, J. Mattingly, and C. Marek. Performance cycle analysis of a two-spool, separate-exhaust turbofan with interstage turbine burner. 07 2005.

[41] Teik-Cheng Lim and Rakesh Kumar Singh. Vibration transmission through rolling element bearings, part i: Bearing stiffness formulation. *Journal of Sound and Vibration*, 139:179–199, 1990.

[42] Wei-Liem Loh. On Latin hypercube sampling. *The Annals of Statistics*, 24(5):2058 – 2080, 1996.

[43] Osami Matsushita, Masato Tanaka, Hiroshi Kanki, Masao Kobayashi, and Patrick Keogh. *Vibrations of Rotating Machinery*, volume 16. 2017.

[44] Georgios Mitsos. Influence of speed and eccentricity dependent bearing stiffness and damping on rotor vibration. Master's thesis, National Technical University of Athens, 2022.

[45] Georgios Mitsos, Ioannis Chatzisavvas, and Athanasios Chasalevris. Multi-harmonic unbalance response of aircraft jet engine rotors on squeeze film dampers. In *Proceedings of SIRM 2023 - The 15th European Conference on Rotordynamics*, 2023.

[46] Maxime Perreault, Sina Hamzehlouia, and Kamran Behdinan. Application of computational fluid dynamics for thermohydrodynamic analysis of high-speed squeeze-film dampers. *Transactions of the Canadian Society for Mechanical Engineering*, 43(3):306–321, 2019.

[47] Hai Pham and Philip Bonello. An impulsive receptance technique for the time domain computation of the vibration of a whole aero-engine model with nonlinear bearings. *Journal of Sound and Vibration - J SOUND VIB*, 318:592–605, 12 2008.

[48] J.E. Pope. *Rules of Thumb for Mechanical Engineers: A Manual of Quick, Accurate Solutions to Everyday Mechanical Engineering Problems*, 1997.

[49] Python. scipy.optimize.fsolve. `https://docs.scipy.org/doc/scipy/reference/generated/scipy.optimize.fsolve.html`.

[50] Walter Ritz. Über eine neue methode zur lösung gewisser variationsprobleme der mathematischen physik. *Journal für die reine und angewandte Mathematik*, 135:1–61, 1909.

[51] Luis San Andrés, Bonjin Koo, and Sung-Hwa Jeung. Experimental Force Coefficients for Two Sealed Ends Squeeze Film Dampers (Piston Rings and O-Rings): An Assessment of Their Similarities and Differences. *Journal of Engineering for Gas Turbines and Power*, 141(2):021024, 10 2018.

[52] Emmanuelle Sarrouy and Jean-Jacques Sinou. Non-linear periodic and quasi-periodic vibrations in mechanical systems - on the use of the harmonic balance methods. In Farzad Ebrahimi, editor, *Advances in Vibration Analysis Research*, chapter 21. IntechOpen, Rijeka, 2011.

[53] Simon Schneiderbauer and Michael Krieger. What do the navier-stokes equations mean ? *European Journal of Physics*, 35:015020, 01 2014.

[54] D. Scholz. Jet engines - bearings, seals and oil consumption, 2018.

[55] Furkan Sevencan, Ender Cigeroglu, and Özgür Uğraş Baran. Nonlinear vibrations of rotor-bearing systems supported by squeeze film dampers due to unbalance excitation. Volume 7B: Dynamics, Vibration, and Control:V07BT07A043, 11 2021.

[56] J.-J. Sinou. Non-linear dynamics and contacts of an unbalanced flexible rotor supported on ball bearings. *Mechanism and Machine Theory*, 44(9):1713–1732, 2009.

[57] Ino Stylianopoulou. Influence of speed and load dependent bearing stiffness on rotor vibration. Master's thesis, National Technical University of Athens, 2023.

[58] Qingchang Tan and Xiaohua Li. Analytical study on effect of a circumferential feeding groove on unbalance response of a flexible rotor in squeeze film damper. *Tribology International*, 32(10):559–566, 1999.

[59] Felix Tieleman. A review and conceptual application of machine learning methods for aircraft engine rotor optimization. Technical report, 2024.

[60] S.P. Timoshenko. On the correction factor for shear of the differential equation for transverse vibrations of bars of uniform cross-section. *Philosophical Magazine*, page 744, 1921.

[61] S.P. Timoshenko. On the transverse vibrations of bars of uniform cross-section. *Philosophical Magazine*, page 125, 1922.

[62] E Torenbeek and H Wittenberg. *Aircraft Engines and Propulsion*, pages 181–252. Springer Netherlands, Dordrecht, 2009.

[63] Christian Wagner. *Dynamic Modeling of Turbopumps*. PhD thesis, Technische Universität München, 2019.

[64] Kaixiang Wei. Turbofan and turbojet engines: Working process and future development. *Theoretical and Natural Science*, 12:114–119, 11 2023.

[65] J.A. Wensing. *On the dynamics of ball bearings*. Phd thesis - research ut, graduation ut, University of Twente, Netherlands, December 1998.

[66] Gao Yanlei and Zhou Yanpei. Airworthiness management of cfm56 products in faa and easa. *Procedia Engineering*, 17:588–594, 2011. The 2nd International Symposium on Aircraft Airworthiness.

[67] Hailun Zhou, Gangyi Cao, Xi Chen, Yuqi Zhang, and Yangguang Cang. A study on the thermal properties of oil-film viscosity in squeeze film dampers. *Lubricants*, 11(4), 2023.